

CONTINUOUS ELECTRON STIMULATED OXYGEN ATOM EMISSION
FROM Ag PERMEATION MEMBRANES

A Thesis presented to Department of Chemistry
of The College of William and Mary


In Partial Fulfillment
of the Requirements for the Degree of
Master of Arts

By
Gilda A. Miner

April, 1995

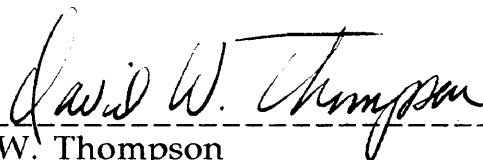
APPROVAL SHEET

This thesis is submitted in partial fulfillment of
the requirements for the degree of
Master of Arts


Gilda A Miner

Approved: April , 1995


R. A. Orwoll


D. W. Thompson

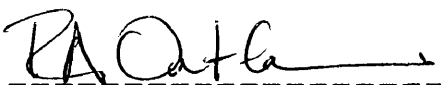

R. A. Outlaw, NASA Langley Research Center

TABLE OF CONTENTS

List of Tables	iv
List of Figures	v
Acknowledgement	vi
Abstract	vii
Introduction	2
Chapter I: The Atomic Oxygen Generator	4
A. The Concept	4
B. Theory of Operation	3
C. Previous Research	9
Chapter II: The Experimental System	11
A. The Construction of the Atomic Oxygen Source	11
B. Ultrahigh Vacuum Apparatus and Detection System	15
C. UHV System Preparation	17
D. System Evacuation	21
E. Initial Instrument Evacuation	22
F. Calibration of the System	26
Chapter III: Experimental Procedures	31
A. Oxygen Flux Calculation	31
B. Modes of Operation	31
Chapter IV: Results	36

TABLE OF CONTENTS
Continued

Chapter V: Discussion	48
A. Flux Measurements	48
B. Permeation Limitations	49
C. O/Ag (poly) ESD Cross-Section	51
Chapter VI: Conclusions	52
References	54
Appendix A: A Survey of Atomic Oxygen Generators	58
Appendix B: Determination of the Work Function for Circular Thoria Coated Tungsten and Iridium Filaments	71
1. Introduction	71
2. Filament Cleaning Procedures	73
3. Coating Procedures	74
4. Work Function Experiment	74
5. Results	74
Appendix C: Ion Gauge and Quadrupole Mass Spectrometer	80
1. Ion Gauge	80
2. Quadrupole Mass Spectrometer	83
VITA	87

LIST OF TABLES

Table 1: Calibration Report for Ion Gauge	27
Table 2: First Ionization Potential of Selected Species	34
Table A-1: Atomic Oxygen Test Facilities	59
Table B-1: Table of Work Functions for Some Metals	73

LIST OF FIGURES

1. Concept Illustration	5
2. ESD Excitation Mechanism	7
3. Schematic of Atomic Oxygen Source	12
4. Illustration of Oxygen Source Assembly	14
5. Illustration of Experimental System	16
6. Photograph of Experimental System Instrumentation	18
7. Photograph of Experimental System(Back View)	19
8. Photograph of Experimental System (Close up)	20
9. Plot of Filament Heating vs. Filament Current	23
10. Plot of Lens Bias Voltage vs. Filament Current	24
11. Initial Mass Scan of Experimental System	25
12. Illustration of Experimental System for Ion Gauge Calibration	28
13. Plot of Corrected Ion Gauge Current vs. Mass Spec Current	29
14. Peak Height As a Function of Emission Current	33
15. Mass Spectra of Normal Mode, AP Mode, RIEM	37
16. Variation of O with ESD Cycled On and Off	38
17. Variation in Species as a Function of ESD Current	40
18. Plot of Detected Flux vs. ESD Current for a Family of Voltages	41
19. Atomic Oxygen Flux as a Function of Electron Energy	42
20. Arrhenius Plot of Atomic Oxygen Flux	43
21. Plot of Ion Currents vs. Time	45
22. Plot of Oxygen Flux vs. Distance from the Detector	46
A-1. Illustration of Atomic Oxygen Test Facilities	59
A-2. Los Alamos National Laboratory Atomic Oxygen Generator	67
A-3. Diagram of an RF Plasma Asher	69
B-1: Filament Coating Process	75
B-2: Filament Experimental Diagram	76
B-3: Richardson Plot of Thoria Coated Tungsten	77
B-4: Richardson Plot of Thoria Coated Iridium	78
C-1: Ion Gauge Diagram	81
C-2: Diagram of Quadrupole Mass Spectrometer	83
C-3: Illustration of a Mass Scan	85

ACKNOWLEDGEMENTS

I would like to thank the following people for their support during my research: Dr. R. A. Outlaw for accepting me into his research group, giving me the opportunity to work on the improvements of his invention (the Hyperthermal Oxygen Atom Generator), taking time away from his research to teach me the basics in vacuum technology, providing daily nudges and encouragements, and most of all, for his friendship for the many years before and since I have had the opportunity to work with him. Dr. Robert A. Orwoll, my advisor, whose Polymer Chemistry class for Secretaries started me on this long road and has been there when I needed him through many research starts and stops. Dr. Dongchuan Wu and Mr. Quinton Duncan for helping me with the experimental apparatus when I was in a panic and nothing seemed to be working right and for taking data when I couldn't. Mr. John R. Gleason for his technical support and the assembly of the generator. Mrs. Lois Forbes for her highly appreciated technical support on this and other research and for her friendship. Mrs. Anne St. Clair for allowing me to complete this work after being assigned to her research group. My mother, Mrs. Ouida Newton Wright who was not able to complete high school, but encouraged me and my siblings to complete our education and stressed the importance of a good job, especially for her daughters.

ABSTRACT

The emission characteristics of atomic oxygen generated by electron stimulated desorption (ESD) from the downstream surface of a polycrystalline Ag membrane have been studied. The oxygen is supplied by permeation through the membrane where it emerges into an atomically bound state at the downstream ultrahigh vacuum surface and then is desorbed by ESD. The flux levels of atomic oxygen were approximately linear with electron bombardment current and measured up to approximately $1 \times 10^{14} \text{ cm}^{-2} \text{ s}^{-1}$ (electron bombardment flux of 20 mA cm^{-2} at 400V) at the emission plane. Reaction products, such as CO, tracked the increasing O flux with ESD current while the O_2 from permeation decreased. An Arrhenius plot of the flux showed linearity up to 475°C where the surface concentration for oxygen adatoms became a constant. The cross section for the ESD process was determined at different emission currents and found to be $4.5 \times 10^{-18} \text{ cm}^2$ which is large compared to other systems. The oxygen atom to ion ratio emitted was determined to be in excess of 1×10^6 , but the specific ESD mechanism in operation is still under study.

CONTINUOUS ELECTRON STIMULATED OXYGEN ATOM EMISSION
FROM POLYCRYSTALLINE Ag

INTRODUCTION

For the last two years, the High Energy Science Branch at NASA, Langley Research Center has been investigating the combined mechanism of oxygen permeation and electron stimulated desorption (ESD) to generate a continuous flux of hyperthermal atomic oxygen. The initial direction of this work was to develop an oxygen generator for investigating the effects of atomic oxygen on space materials in a laboratory environment and to determine the reaction cross-sections and reaction rates from scattering data of a cross beam of ground-state oxygen atoms and ground-state or excited nitrogen molecules.

The composition of the atmosphere within the orbital envelope (200-1000 km) combined with the orbital velocity ($\sim 8 \text{ km s}^{-1}$) results in a flux of hyperthermal atomic oxygen ($\sim 5 \text{ eV}$, $\sim 10^{15} \text{ cm}^{-2} \text{ s}^{-1}$) impinging on spacecraft surfaces. The extreme reactivity of atomic oxygen leads to numerous chemical reactions with other species to form CO, CO₂, H₂O, O₂, SO₂, NO₂, and other oxygen species. Further, the high chemical reactivity of this O atom flux has caused substantial degradation of organic materials on the Space Shuttle and the Long Duration Exposure Facility (LDEF) and suggests that materials on the proposed space structures such as, the proposed space station, may have reduced lifetimes. It is, therefore, essential to study the reactivity of these materials to atomic oxygen in ground based laboratories.¹⁻³

Cross-beam experiments require mono-energetic beams that are well defined as to atomic flux, energy distribution, and internal energy. The

original O-source invented and developed at NASA produces O atoms, O⁺ ions, and O₂ molecules. The maximum flux of this oxygen source is on the order of $1 \times 10^{14} \text{ cm}^{-2}\text{s}^{-1}$ with a kinetic energy of approximately 5 eV, full width at half maximum (FWHM) of 4 eV. No parametric measurements have been made with this source. This work encompasses a partial characterization of this O-atom source in order to better understand the generated beam. The characterization will then, in turn, permit a better understanding of space materials degradation experiments and cross beam reaction rates and cross-sections for refinement of hypersonic codes.

CHAPTER I

THE ATOMIC OXYGEN GENERATOR

A. THE CONCEPT

The concept of the hyperthermal oxygen atomic generator is illustrated in figure 1. Two regions are separated by a heated polycrystalline Ag membrane. The upstream region is comprised of molecular oxygen between 1 and 1000 Torr of pressure. The downstream region is a high or ultrahigh vacuum (UHV) region within which the atomic oxygen beam is formed.

In the upstream region, the molecular oxygen dissociatively adsorbs onto the heated Ag membrane and dissolves in the octahedral holes of the Ag lattice. The oxygen atoms diffuse (under the influence of a concentration gradient) through the bulk to the downstream (UHV) interface where the emerging oxygen atoms enter into an atomically bound state. Simultaneously, the downstream surface of the membrane is bombarded with a uniform flux of electrons which desorb a fraction of the adatoms by ESD and create a flux of hyperthermal oxygen atoms. The theoretical limit of this flux is determined by the supply of atoms arriving at the UHV interface permeation.

B. THEORY OF OPERATION

Oxygen has an unusually high permeability through silver and its alloys.⁴ Silver oxide is not spontaneously formed and does not create a barrier on the surface as for example, aluminum oxide does on aluminum.

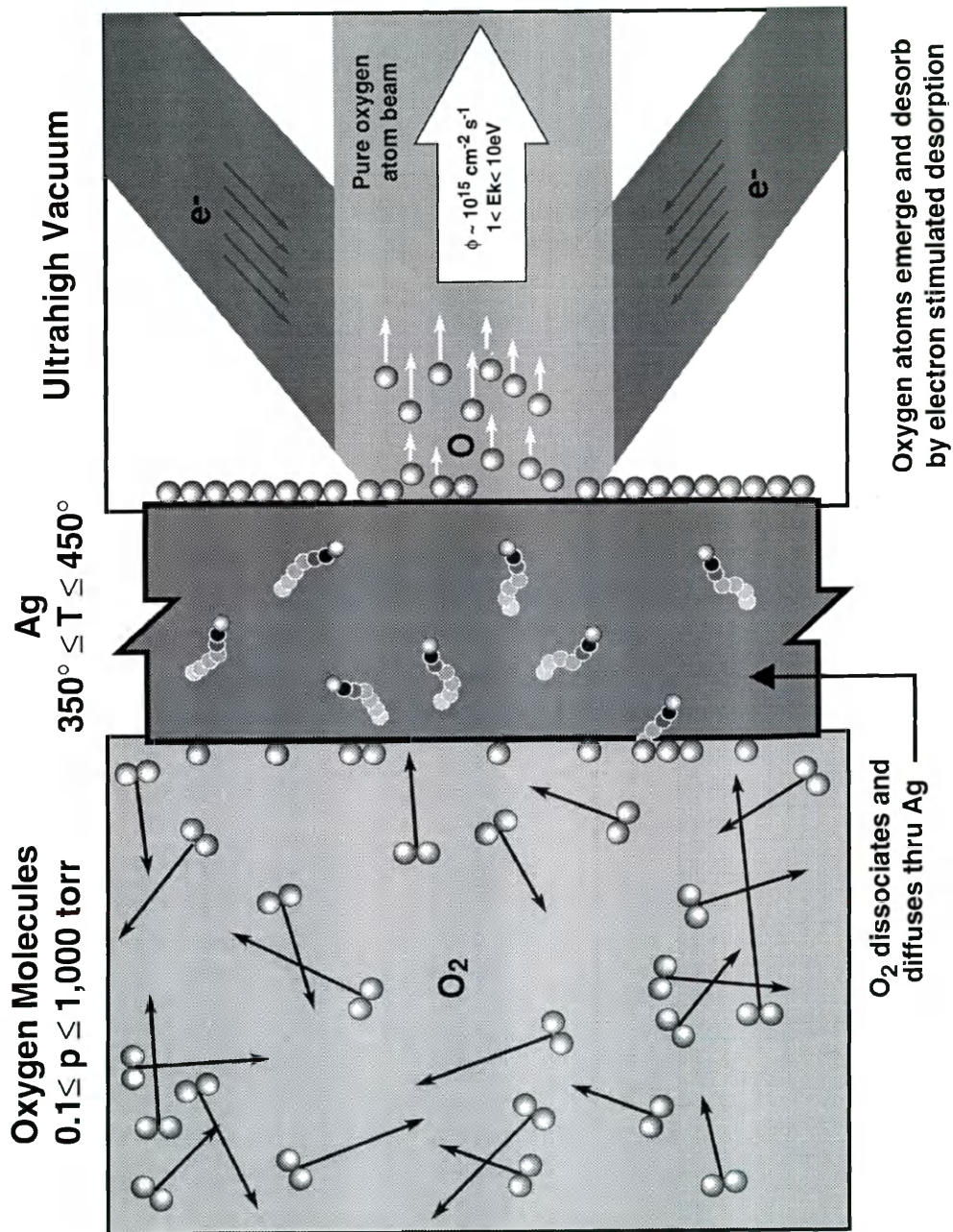


Figure 1. Illustration of the concept of atomic oxygen generation.

The O₂ molecule adsorbs and dissociates into atoms at the Ag surface and then subsequently dissolves into the solid state lattice. Since atomic oxygen is only slightly larger than the octahedral holes of the silver (atomic radius = 0.06 nm), it readily jumps from octahedral hole to octahedral hole and diffuses through the membrane. The rate of diffusion is controlled by the solid temperature and by the concentration gradient. Steady state diffusion is described by Fick's first law:

$$J = -D \left(\frac{\partial C}{\partial x} \right); \quad (1)$$

where J is the flux of oxygen through the silver, D is the diffusion coefficient, C is the concentration of oxygen, and Δx is the thickness of the membrane.

At membrane temperatures below $\sim 550^\circ \text{C}$, the atoms emerge at the vacuum interface and enter into stable atomically bound states at the surface. At membrane temperatures above $\sim 550^\circ \text{C}$, the oxygen atoms arriving at the interface have sufficient thermal energy for surface diffusion which results in recombination and desorption as O₂ molecules.⁵ All data in this thesis was taken below 550°C .

The mechanism of ESD at the downstream interface involves the use of an incident flux of low energy electrons ($E < 3 \text{ kV}$) to excite the bound atoms to antibonding states which desorb as O neutrals with kinetic energy of about 5 eV. Figure 2 shows the interaction potential of oxygen adatoms on the surface and the subsequent change in that potential to any of three possible potentials due to electron stimulation. Although there are numerous theories that describe different desorption mechanisms, a probable

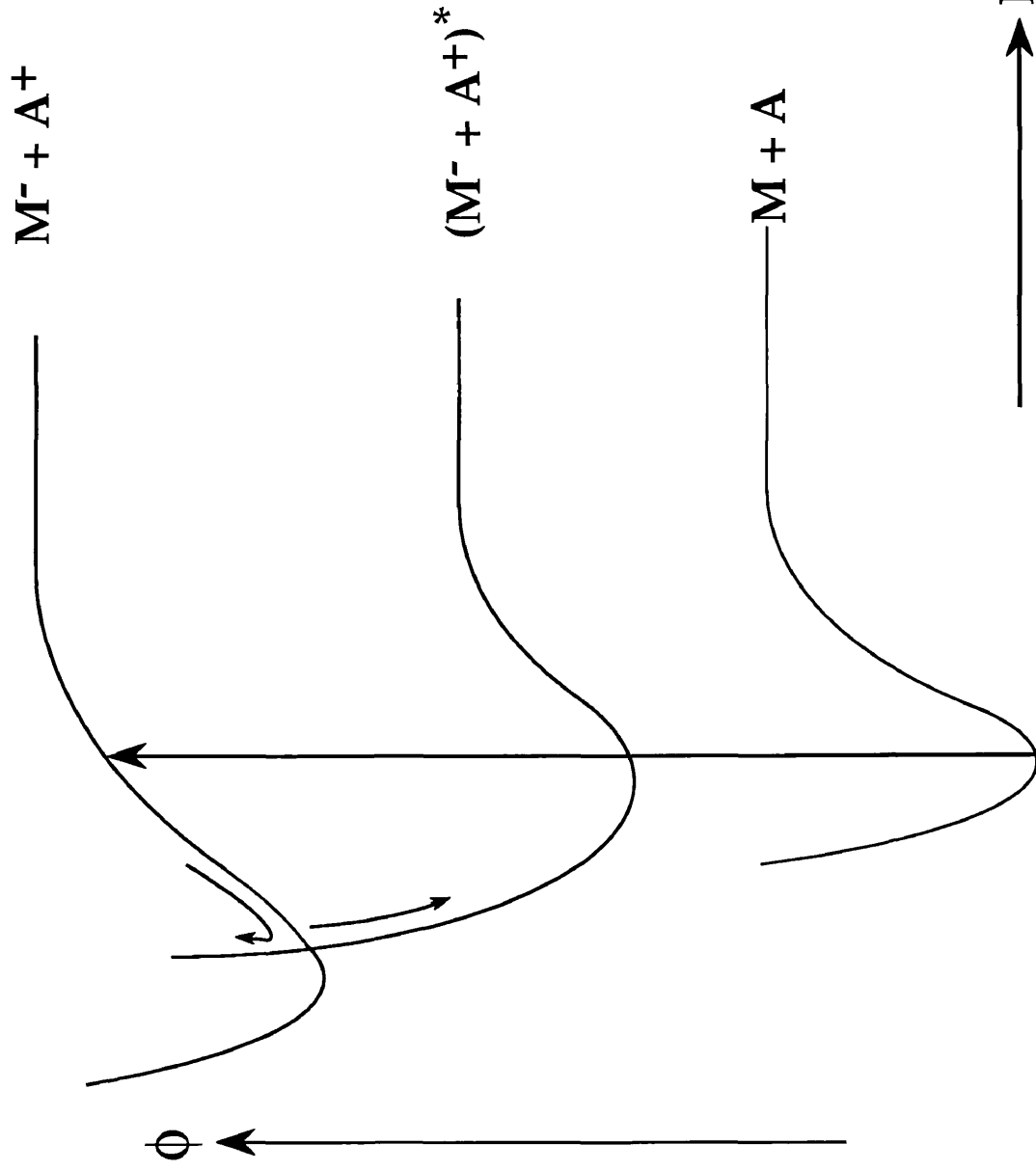


Figure 2. Illustration of the ESD excitation mechanism. R represents intermolecular distance in arbitrary units, ϕ is the potential energy in arbitrary units, M is the metal ion/atom, and A is the adsorbed ion/atom.

scenario for ESD of oxygen from Ag is that of the Antoniewicz mechanism.⁶ In this case, the adsorbed oxygen is positively ionized and is attracted to the negative image potential in Ag. As it is accelerated toward this image potential, it is ultimately neutralized by Fermi electrons after having gained an average of ~ 5 eV kinetic energy. At this point, the neutral oxygen atoms are so close to the Ag surface, the repulsion between the electron orbitals of the oxygen and Ag elastically scatter the oxygen neutral away, thus providing the observed flux. The actual energy distribution of these atoms is determined by the position of neutralization.

A continuous supply of molecular oxygen on the upstream side of the silver membrane and a sufficient Ag membrane temperature for O atom transport provides a continuous supply of adsorbed oxygen atoms for ESD. For optimum operation, the Ag must be operated at a temperature high enough to ensure a sufficient oxygen permeability, but low enough that the atomic adsorbed state is stable, and molecular oxygen is not formed. The surface coverage of oxygen atoms downstream at the UHV interface is given by

$$-\sigma_O \frac{d\theta}{dt} = J_{O/Ag} - J_{O/ESD} \cdot \quad (2)$$

where θ is the relative surface coverage, $J_{O/Ag}$ is the oxygen atom flux through the Ag, $J_{O/ESD}$ is the electron stimulated desorption of oxygen, and σ_O is the monolayer surface concentration ($\sim 2.4 \times 10^{15} \text{ cm}^{-2}$).² The flux is determined primarily by the membrane temperature, thickness, and upstream pressure for the transport and by electron bombardment flux and energy for ESD.

C. PREVIOUS RESEARCH

There are numerous methods of generating atomic oxygen, e.g.. radio frequency (rf) discharge, laser and thermal dissociation, and electron impact ionization. In order to attain a range of energies, several methods of acceleration, such as electrostatic (followed by charge transfer) and nozzle expansion, are used. Beams formed through the use of these techniques have some combination of the following problems: low flux, low mean energy, wide energy distribution, numerous excited states of oxygen and accompanying gases, and synergistic reactions from different species. Furthermore, contaminating background densities within the experimental system often mask the true interaction between atomic oxygen and the material sample. In the vast majority of these systems, they are large complex units that are not UHV compatible and not amenable to a laboratory system retrofit. An overview of these systems can be found in Appendix A.

The initial work for the method of generating atomic oxygen presented here made use of the unique phenomenon of atomic oxygen diffusing through silver and ESD to demonstrate the proof of concept.⁷ In this work, the authors used a Ag wire charged with $^{16}\text{O}_2$ (a second part of experiment verifying the concept used $^{18}\text{O}_2$) and bombarded it with low-energy electrons (≈ 100 eV) under UHV conditions. Atomic O flux levels of $1 \times 10^{12} \text{ cm}^{-2} \text{ s}^{-1}$ were detected at a Ag temperature of 300° C using a quadrupole mass spectrometer operating in the appearance potential mode.

The development of the first compact UHV compatible instrument using the aforementioned technique was reported in the May/June 1994 issue

of Journal of Vacuum Science Technology.⁸ The reported flux of neutral O atoms was $4.5 \times 10^{13} \text{ cm}^{-2} \text{ s}^{-1}$ detected from a quadrupole mass spectrometer located 10 cm downstream.

CHAPTER II

THE EXPERIMENTAL SYSTEM

A. THE CONSTRUCTION OF THE ATOMIC OXYGEN SOURCE

A schematic of the oxygen generator is shown in figure 3. The molecular oxygen is supplied on the inside of the tube that connects with the Ag "top hat" geometry. The "top hat" is heated internally by a cylindrical heater (not shown in the schematic). Between the heater and the bombardment of the electrons, the membrane can reach temperatures of 20 to 800° C. The Ag membrane thickness for this study is 300 μm. A more detailed diagram of the "top hat" is shown in the inset of figure 3. The circular filament is thoria (thorium oxide) coated tungsten, see Appendix B. The filament is positioned below the Ag membrane surface in order to eliminate line of sight contamination from the filament to the silver membrane surface. Previous configurations of the gun had the filament positioned above the membrane surface. A repeller lens is positioned over the Ag membrane "top hat" and the filament which repels the electrons from the filament and deflects them towards the membrane creating a uniform flux of electrons onto the Ag membrane. The filament can be biased 0.1 to 2 kV below ground and the lens is slightly more negative to help spread the electron emission. At each electron energy, the lens voltage bias has to be adjusted to insure the most uniform bombardment.

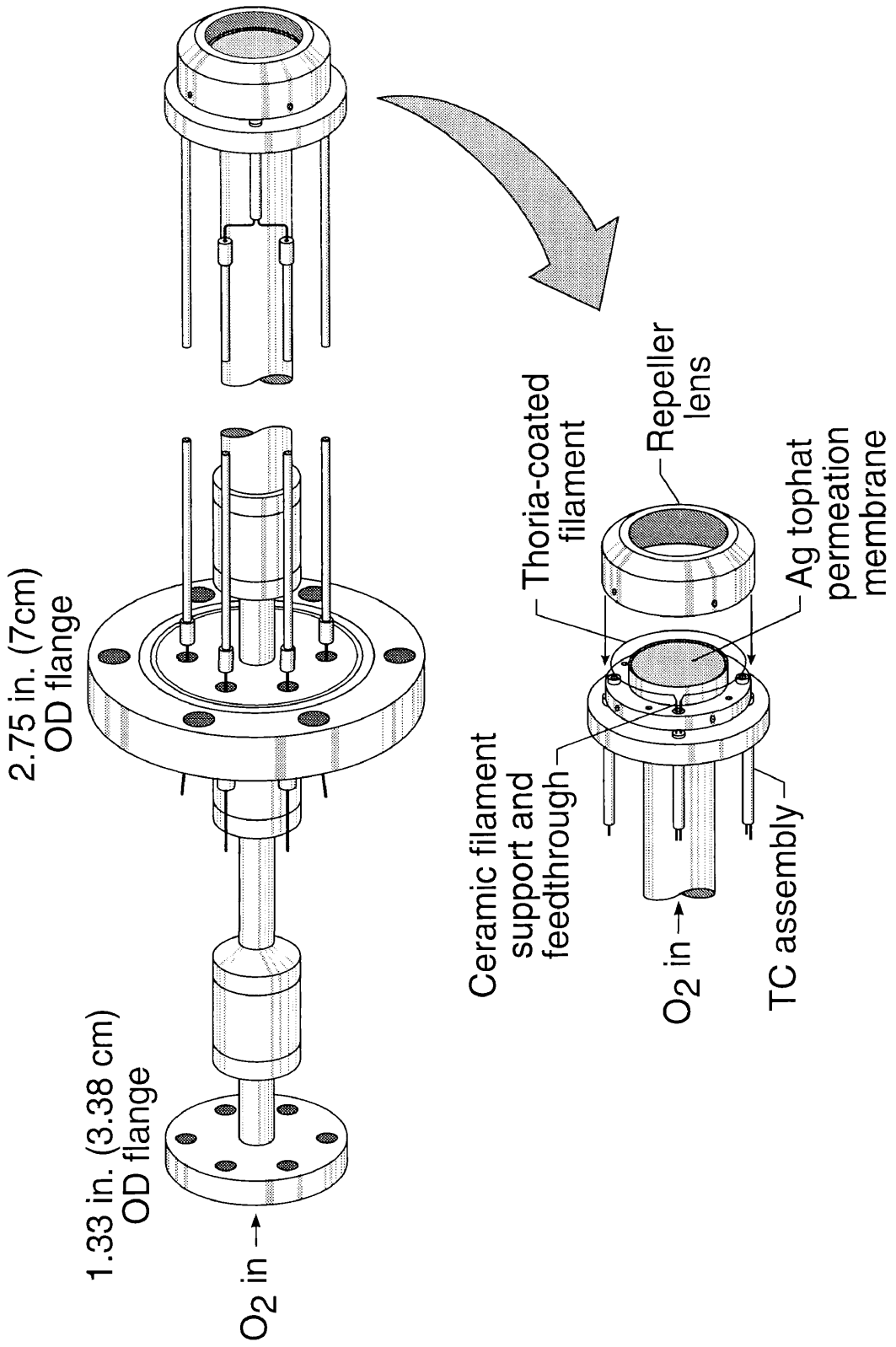


Figure 3. Illustration of the atomic oxygen gun with a close-up view of the "tophat."

The oxygen source studied here utilizes a unique "top hat" design (see figure 4). The "top hat" is machined from 99.99% silver. The sides, lip, and inside were machined first; then, the top membrane was faced off. A special device was designed to hold the "hat" while the inside was machined and the membrane faced off. Because of the precise membrane dimensional requirement and the difficulty of working with a soft material with a reasonably low melting point (962° C), small cuts and special cooling were required. Eight holes were drilled in the "top hat" lip to secure the repeller lens, to insulate the repeller lens from the "top hat," and to provide passage for the thermocouple leads, and high voltage leads to the filament and the lens. After machining, the silver components were vacuum fired by placing them in a vacuum oven with pressures in the 10^{-6} to 10^{-7} Torr range and heated to 800° C. The thermocouple and electrical leads were insulated with alumina and were run along the sides of the O₂ supply tube and attached with barrel connectors to the leads in the UHV flange.

The barrel was assembled by first silver brazing a 3" section of 1/2" O.D. silver tubing to the "top hat." An 8-1/2" length of 1/2" O.D. copper tubing was silver braised to the silver tube. Prior to brazing, the copper tubing was vacuum fired similar to the silver components; however, the temperature was only taken up to 600° C. The purpose of changing to copper tubing was to reduce cost and to conduct heat from the "top hat" and membrane (this length of the copper tubing can vary according to the needs of the system). The overall length of this gun was 13-5/16". The 1/2" O.D. copper tubing was necked down using a standard copper plumbing fitting to 3/8" copper tubing that was brazed into a standard 2-3/4" UHV flange.

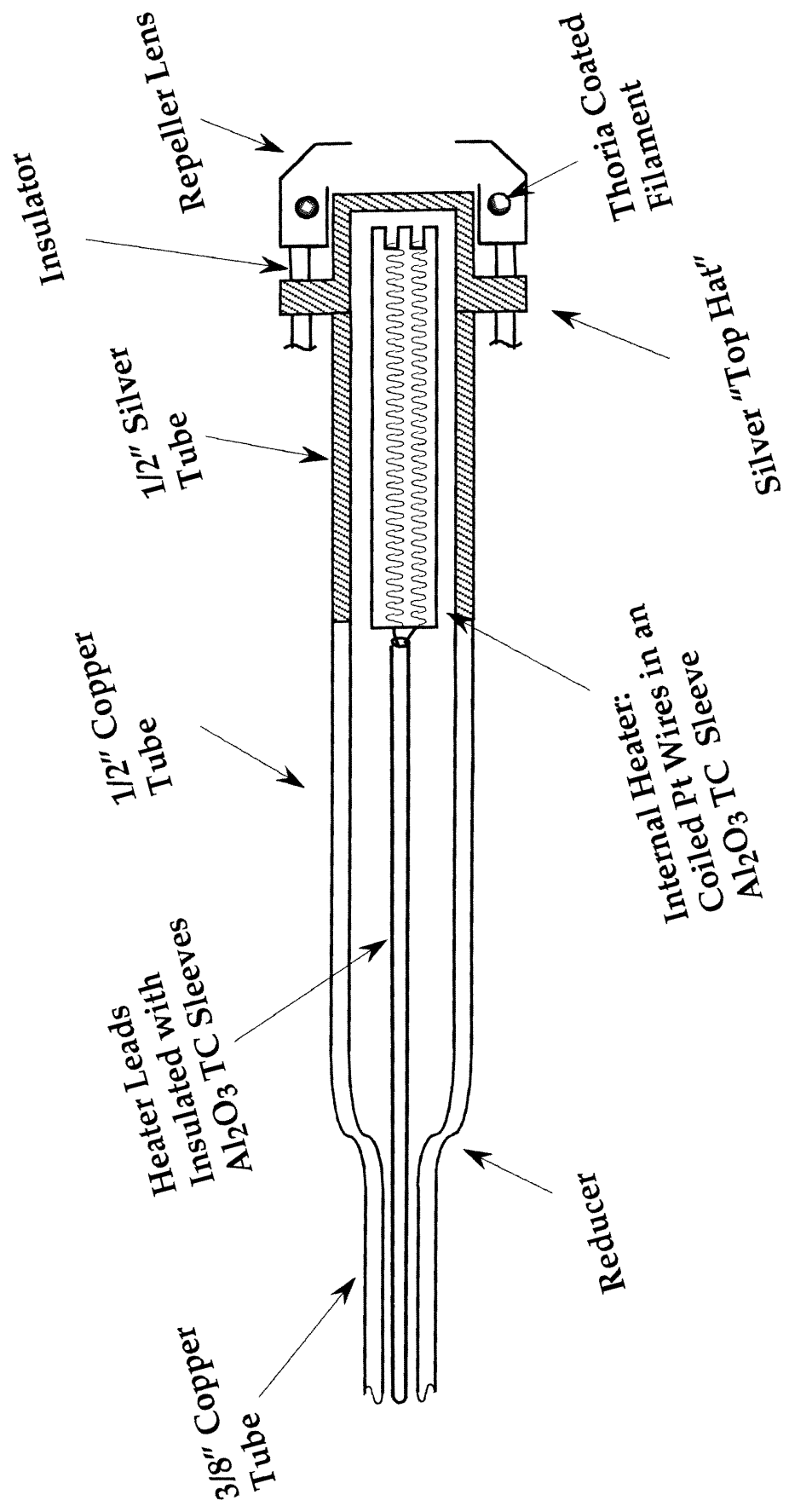


Figure 4. Illustration of the oxygen source with its unique "top hat" design and the tubing configuration to the UHV flange.

The second modification made to the atomic oxygen source was the use of an internal heater. The heater was made from 0.010" diameter platinum wire that was coiled on a 0.020" diameter mandrel. Approximately 4" of coiled platinum wire was needed. Once the wire was coiled and removed from the mandrel, it was stretched slightly so that it could fit into a 0.040" diameter hole of alumina. Approximately 2" of 4-hole 3/8" O.D. alumina was machined down to 1/4" O.D. One end of the alumina was notched from one hole to the hole diagonally across from it. The coiled platinum was then threaded through one hole, into the notch, and down the opposite hole. Recessing the heater into the notch protected the platinum heater coil from damage while the heater was inserted into the oxygen source. The other two holes were used for the 0.06" diameter Cu power leads. The heater was inserted into the gun barrel just behind the silver membrane.

An insulator was placed beyond the 2-3/4" UHV flange outside the UHV oxygen chamber to electrically insulate the gun from the rest of the system. A standard 1-1/3" UHV mini-flange and T-connector was placed beyond the insulator. The internal heater leads exited from the top of the T and the molecular oxygen source entered from the stem of the T connector.

B. THE ULTRAHIGH VACUUM APPARATUS AND DETECTION SYSTEM

The experimental system is composed of the oxygen atom source and a detection system separated by an all-metal seal UHV valve. The valve provides the option of exchanging either the oxygen source or the detection system without opening the other section to the atmosphere. A schematic of the system is shown in figure 5. Not shown in this schematic are the

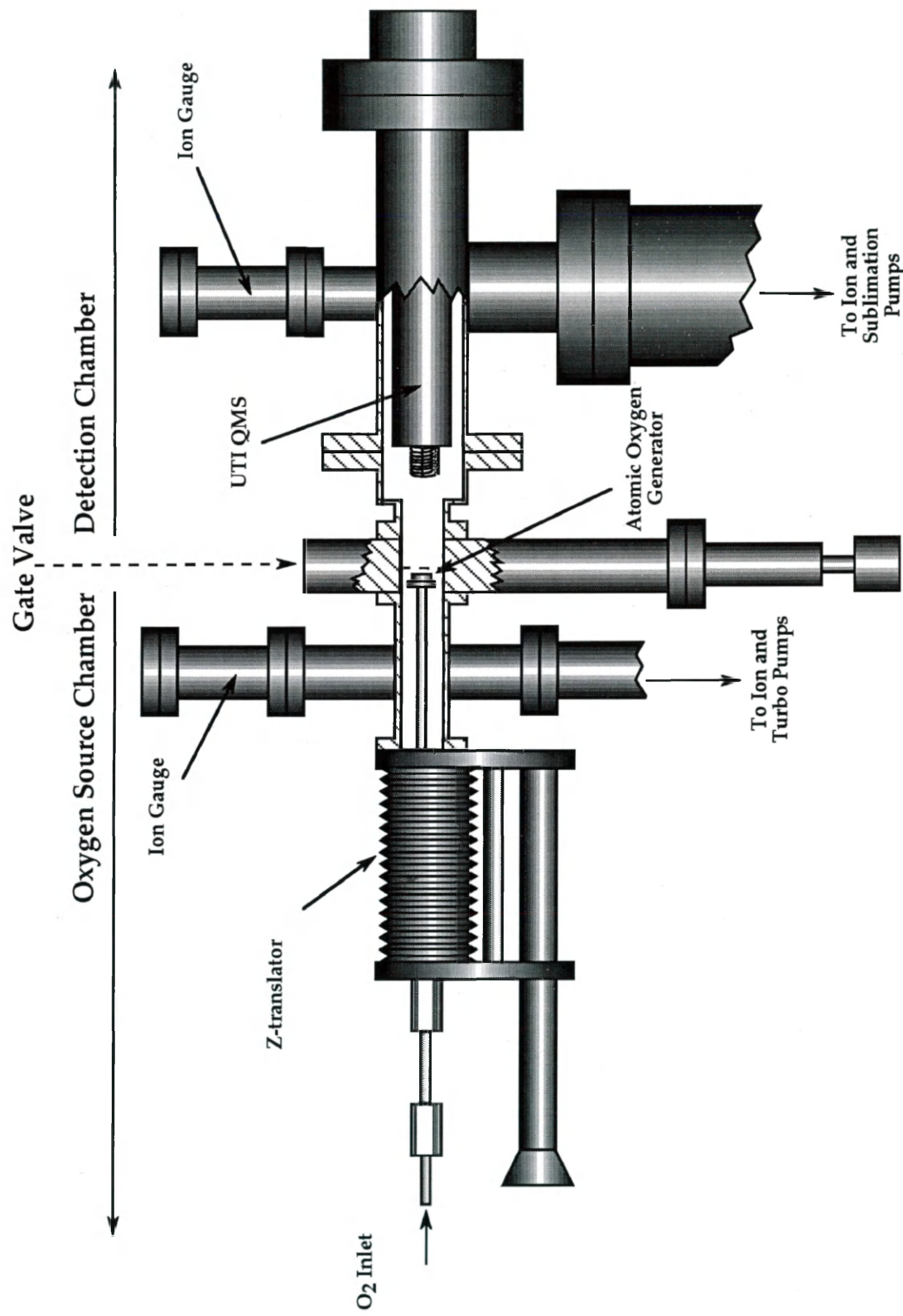


Figure 5. Illustration of the experimental system showing the two sections: the oxygen source chamber and the detection chamber separated by a gate valve.

numerous power sources, ion gauges, readouts, and pumps (roughing, ion, and turbo) with a footprint of approximately 66 square feet. Figure 6 is a photograph of the front side of the experiment. At the far left hand side of the photograph is the strip chart for recording the mass spectra from the UTI mass spectrometer. Just to the right is an instrument rack containing the UTI control unit, pressure gauge readouts, and the control panel for the titanium sublimator. Between the power racks is a table supporting the two high voltage supplies for the reflector lens and the filament. On the power rack to the far right is the Dycor quadrupole mass spectrometer control panel and monitor, variacs, and power readouts.

Figure 7 shows the back side of the experiment. The most prominent objects are the two ion pumps. The center cross is the quadrupole for the UTI mass spectrometer (approximately two inches from the left side). Figure 8 is a close-up view of oxygen source chamber, isolation valve, and detection chamber from the instrumentation side. The Dycor quadrupole is located in the center of the photograph. The oxygen source is located to the right of the cross; the electrical leads can be seen coming from the insulating shield attached to the back of the oxygen source coming from the z translator.

C. UHV SYSTEM PREPARATION

Vacuum components (flanges, crosses, T's, etc.) used in this system were ultrasonically cleaned in a solution of Sparkleen (or Alconox) and hot deionized water for fifteen minutes. The components were then rinsed in fresh deionized water three times, immersed in ethanol, slowly drawn from the ethanol to provide a vapor rinse, and dried with a hot air gun. Water

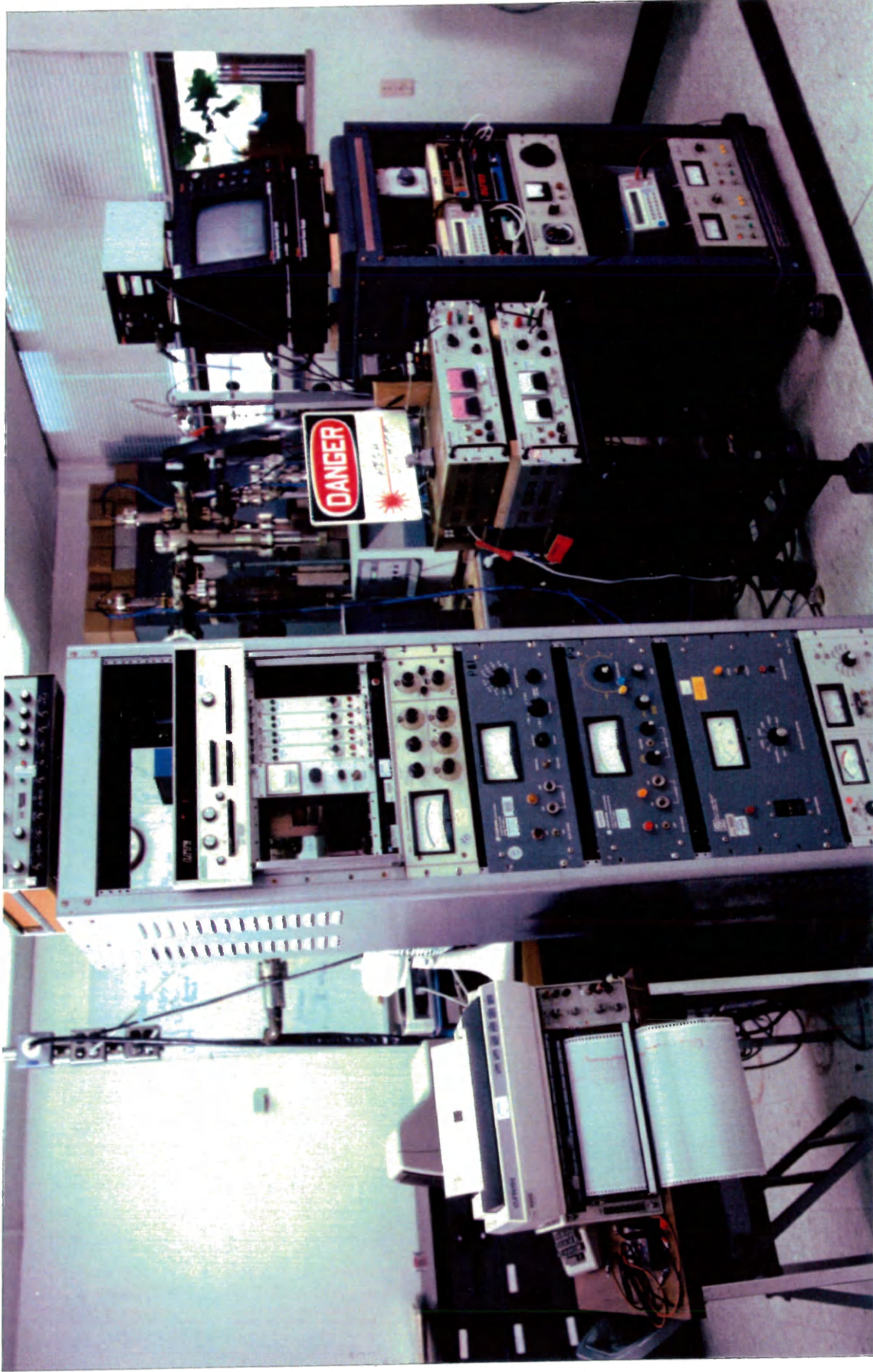


Figure 6. The front of the experimental system showing the instrumentation.

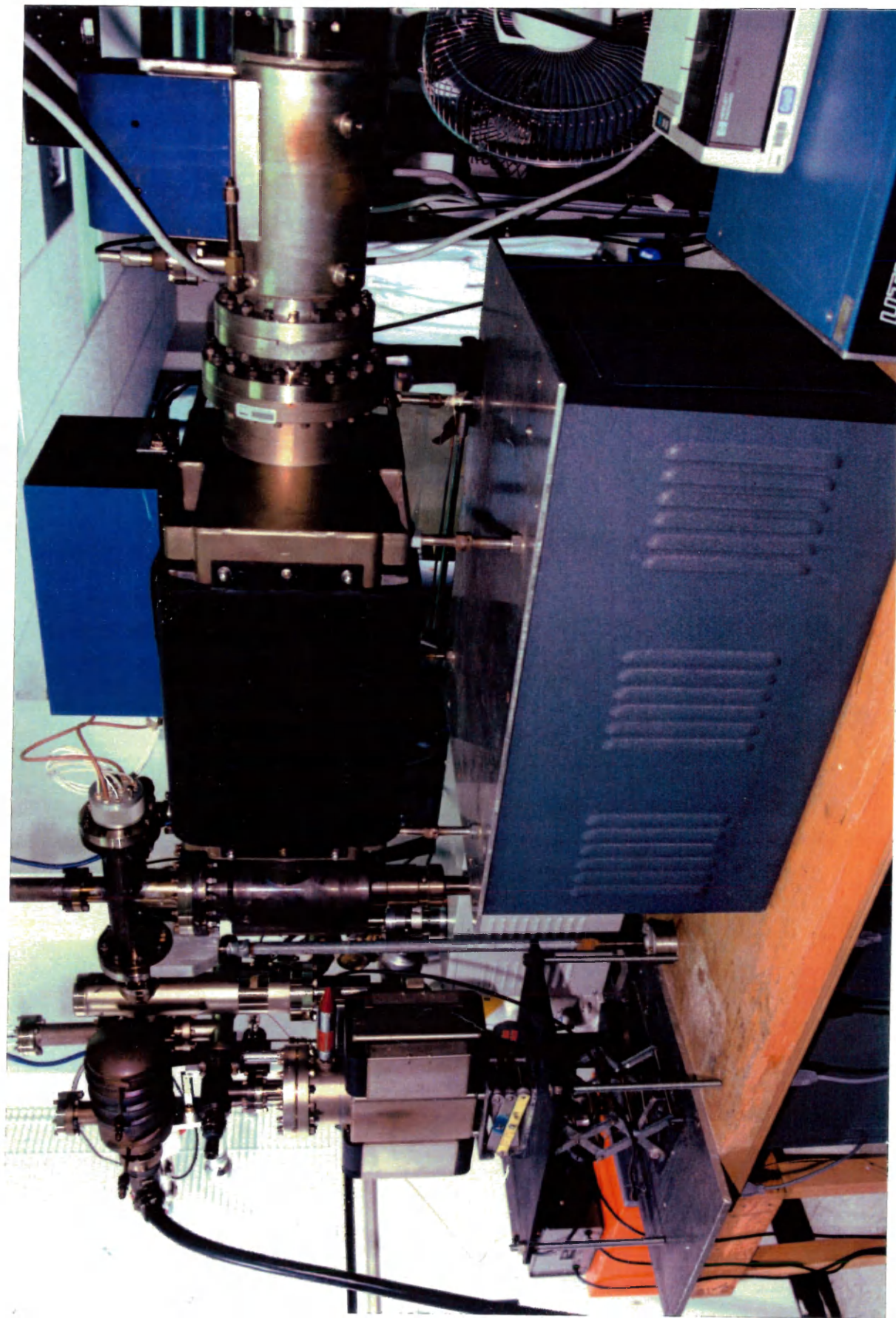


Figure 7. A back view of the experimental system showing two ion pumps. The oxygen source is hidden in this view; however, the gate valve and quadrupole mass spectrometer can be seen in the top left one-third of the photograph.

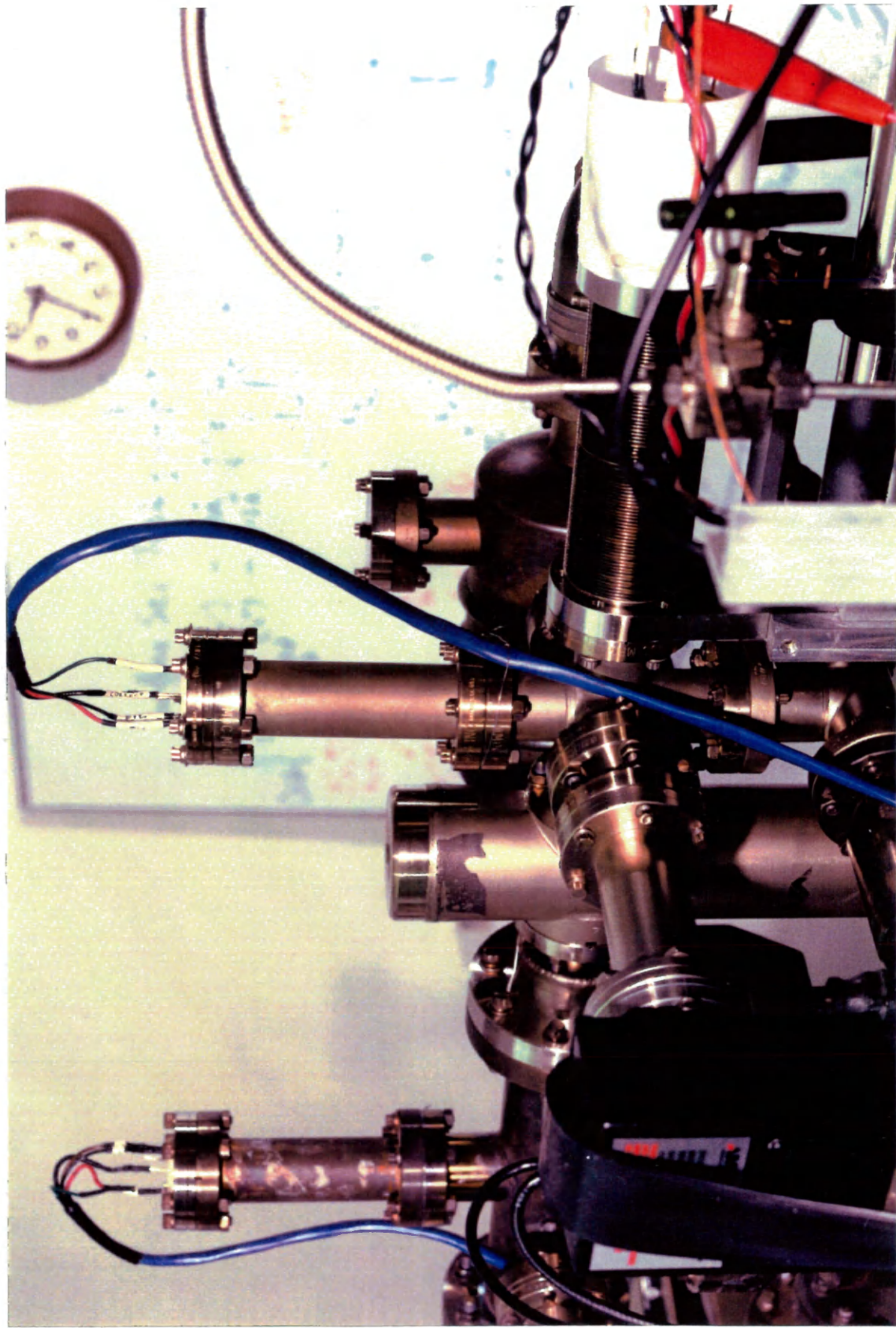


Figure 8. The two prominent features are the ion gauge in the detector chamber (far left) and the ion gauge in the oxygen source chamber (center). The gate valve is located to the left of the oxygen source chamber ion gauge and the oxygen source is housed in the bellows located in the lower right hand corner.

break testing was performed on microscope slides that were cleaned along with the vacuum component to determine the extent of component's cleanliness. A break test consists of dropping deionized water on the cleaned microscope slide: if the deionized water spread sheets off the tilted slide, the component is clean; if the water beads up, the component still has contamination and requires additional cleaning. The vacuum components were then stored in oil-free aluminum foil until placed on the system.

D. SYSTEM EVACUATION

Oil free roughing pumps were used on the oxygen source side of the main valve and on the internal area of the gun to bring pressures into the 10^{-3} to 10^{-4} Torr range. The detection side of the system had been used in prior research and had been kept under vacuum. The ion pump on the detection system side was isolated, heated, and exhausted through a turbo pump. The initial pressure for this system was 2.3×10^{-7} Torr. Both the detection and the gun chamber were baked out with each chamber achieving initial pressures in the 10^{-10} Torr range after the systems were cooled. Eventually, ultimate pressures in the 10^{-11} Torr range were achieved after several over night programs of titanium sublimation were conducted.

The UTI mass spectrometer was operated for 45 minutes with an emission current of 0.5 mA to remove impurities from the filter chamber and filament (a detailed description of the UTI quadrupole mass spectrometer is found in Appendix C). The four filaments of the titanium sublimator were operated at 45 A for 1 minute each to trap impurities. This procedure was repeated until the detection system achieved a pressure of 6.8×10^{-11} Torr.

Likewise, a titanium sublimator was cycled at 35 A for 1 minute in the gun chamber and the atomic oxygen gun filament was degassed. The gas lines to the interior of the oxygen gun were baked out while the electrical connections were between the gun and the power sources and thermocouple readout. All instruments were grounded.

E. INITIAL INSTRUMENT EVACUATION

The first objective was to optimize the emission current. The high voltage supplies were turned on to the lens and the filament to establish emission. Figure 9 shows a plot of the filament current vs. the voltage for the filament heating. Figure 10 is a plot of the lens bias voltage vs. the filament emission current. These two graphs were used to determine the optimum filament current. The initial operation of the system was as follows: the filament bias voltage was 1600 V, the offset voltage was 250 V, the lens current was 2 mA, the filament bias current was 1 mA, the pressure in the gun chamber was 1×10^{-7} Torr, the upstream pressure was 327.1 Torr, the membrane temperature was 413° C, the heater voltage was 8.52 V, and the heater current was 2.95 A.

The system was operated with a filament current of 1.3 A, emission of 1 mA, and a membrane temperature of 450° C for a total of 24 hours over 3 days. Figure 11 shows a mass spectrum of the system taken with a Dycor quadrupole located on the upstream side in the gun chamber. Typical species for a recently established UHV system were detected: hydrogen, carbon, water, carbon monoxide, molecular oxygen, and carbon dioxide. Atomic oxygen from the oxygen source was detected, also. The high concentrations of carbon

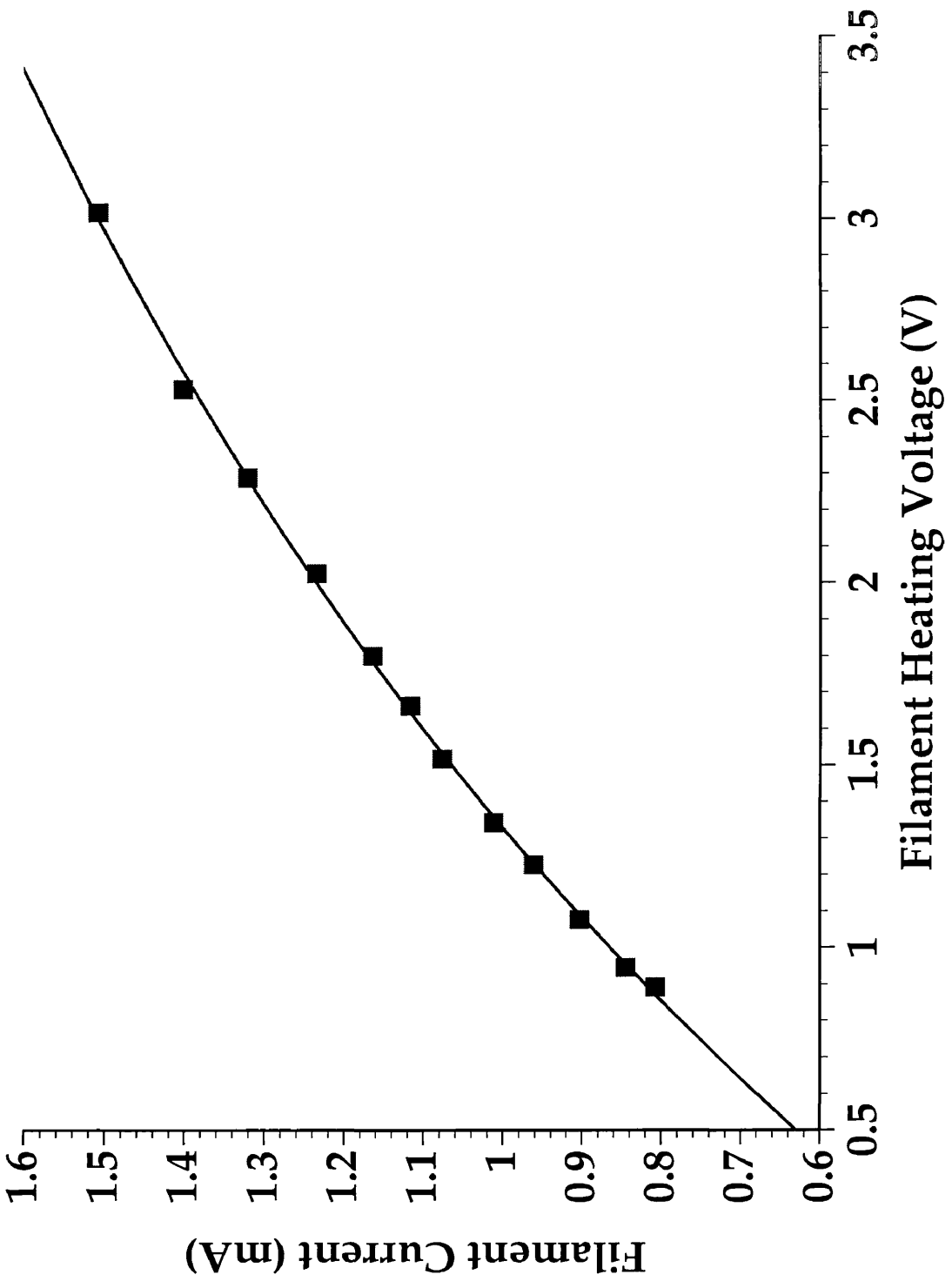


Figure 9. Plot of filament heating voltage vs. filament current to determine optimum filament operation.

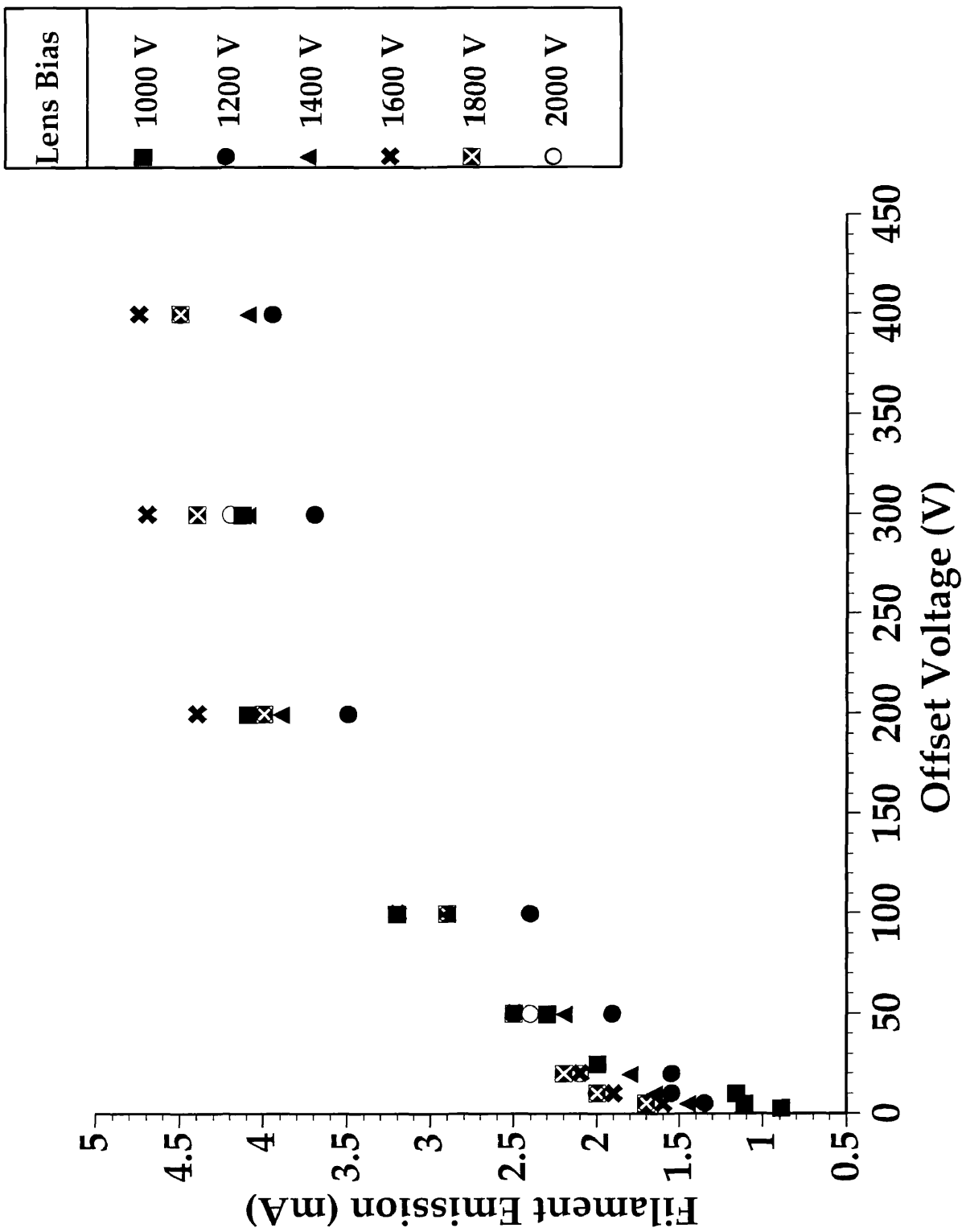


Figure 10. A plot of the offset voltage at various lens bias voltages vs. filament current to determine optimum emission.

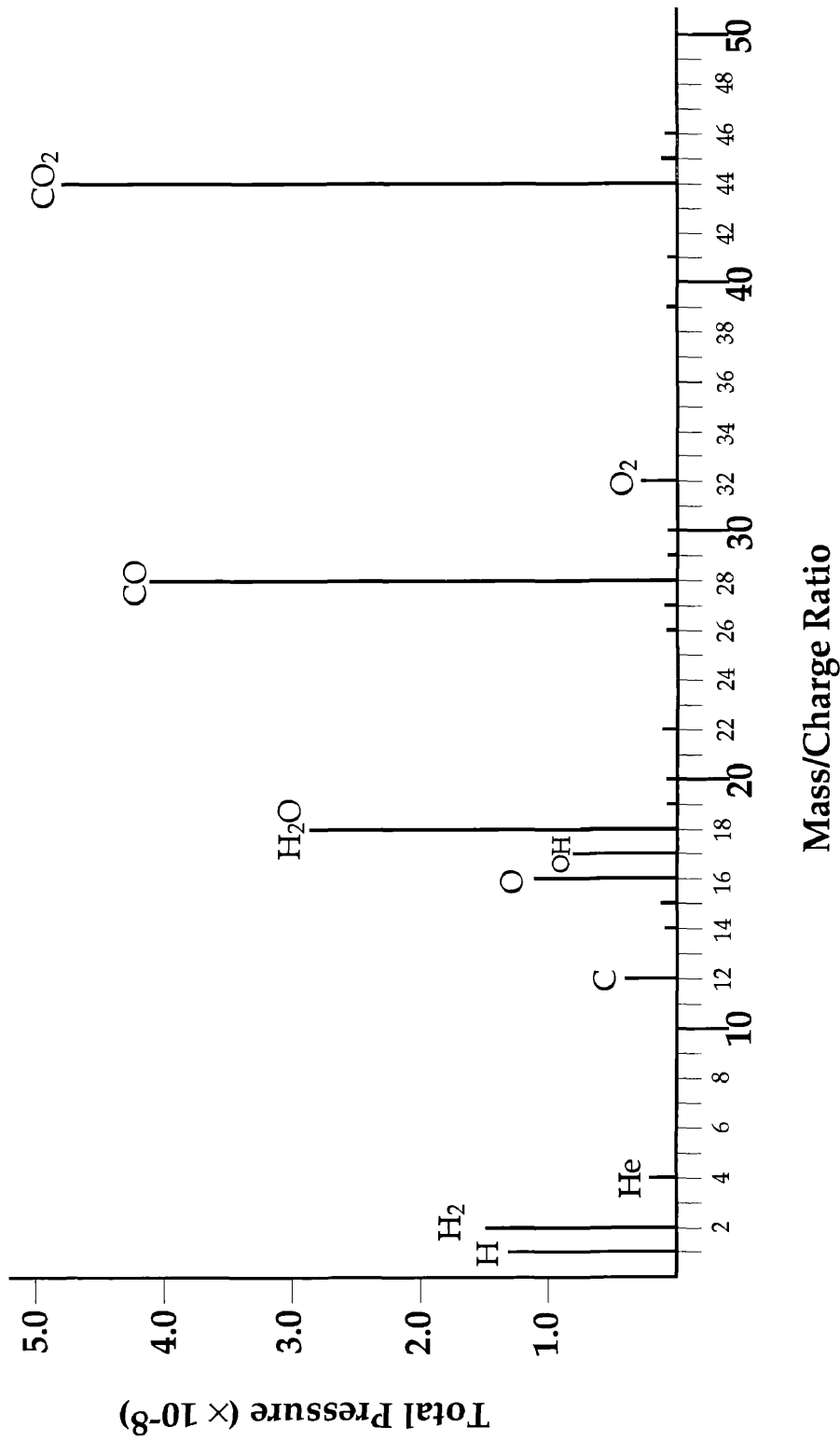


Figure 11. Computer reproduction of mass species in upstream region of system after the first 24 hours of membrane charging.

monoxide and carbon dioxide were from the recombination of carbon and atomic oxygen. With continuous operation the background species declined as a function of time and clean-up. After several days, the background approached a steady state.

F. CALIBRATION OF THE SYSTEM

Calibration of the system was performed using a standard ion gauge which had been calibrated against a spinning rotary gauge using N₂ gas by Wyle Laboratories, Hampton, Virginia. The calibration data are presented in Table 1. The gauge constant (K_1) for the standard gauge was obtained by taking the average of the values from column 4 which is 0.461, then multiplied by the correction factor for O₂ gas (0.826). The placement of the standard gauge is shown in figure 12. Therefore, the gauge constant for the standard ion gauge was determined to be 0.381. This value was used for all pressure measurement.

The standard ion gauge was then used to calibrate a second ion gauge and the QMS operating in the RIEM mode at 0.2 mA emission current. The calibration of the QMS to the ion gauge was performed by backfilling the system with O₂ over the pressure range of 10⁻⁶ to 10⁻⁸ Torr. The calibration result is presented in figure 13 and the sensitivity (S_1) was determined to be 0.094 A. The overall QMS sensitivity, S_{O_2} , was found to be 0.101 A/Torr.

The QMS sensitivity for atomic oxygen, S_O , is obtained from S_{O_2} based on the theory that the ratio of the cross-sections for molecular to atomic oxygen is inversely related to the ratio of the square of the ionization potentials:⁹

Table 1

NASA-LRC-EXPERIMENTAL TESTING AND TECHNOLOGY DIVISION
 REPORT OF CALIBRATION-WYLE-LABORATORIES

IONIZATION GAUGE CONTROLLER

MANUFACTURER: VARIAN EXN/MCN: AOO8365 DATE: 9-14-94
 MODEL NO.: L8350301 SER. NO.: BCTAH9008046
 CAL. BY: W-4623 RANGE: 1.0E-04/1.0E-12 TORR
 JOB NO.: 302810 ORDER NO.:

REF STD: MKS SPINNING ROTOR GAUGE MODEL SRG-2, GFE NO. 5622,
 CALIBRATED 7-23-93.

NOTE: CALIBRATION GAS WAS NITROGEN.
 EMISSION STANDARD SET A 0.4 MILLIAMPS
 TEST INDICATION CORRECTED=(TEST INDICATION-TEST
 INDICATION BASE)/STANDARD INDICATION.

STANDARD INDICATION TORR	TEST INSTRUMENT INDICATION TORR	TEST INSTRUMENT CORRECTED TORR	K FACTOR	INSTRUMENT INDICATION MVDC	
-----	1.83E-07	-----	-----	-----	BASE
4.13E-07	3.62E-07	1.79E-07	0.433	4.2692	
7.70E-07	5.38E-07	3.55E-07	0.461	4.4595	
4.66E-06	2.26E-06	2.08E-06	0.446	5.1056	
9.72E-06	4.52E-06	4.34E-06	0.446	5.3533	
1.46E-05	7.30E-06	7.12E-06	0.487	5.6490	
4.37E-05	2.05E-05	2.03E-05	0.465	6.0772	
8.03E-05	4.16E-05	4.14E-05	0.516	6.3025	
1.14E-04	6.73E-05	6.71E-05	0.589	6.5748	

CONVERSION FACTOR 1.00000
 TEST INSTRUMENT TEMPERATURE 22.9 DEG C.
 AMBIENT TEMPERATURE 22.9 DEG C.
 BAROMETRIC PRESSURE 30.202 IN HGA
 HUMIDITY 38 PERCENT.

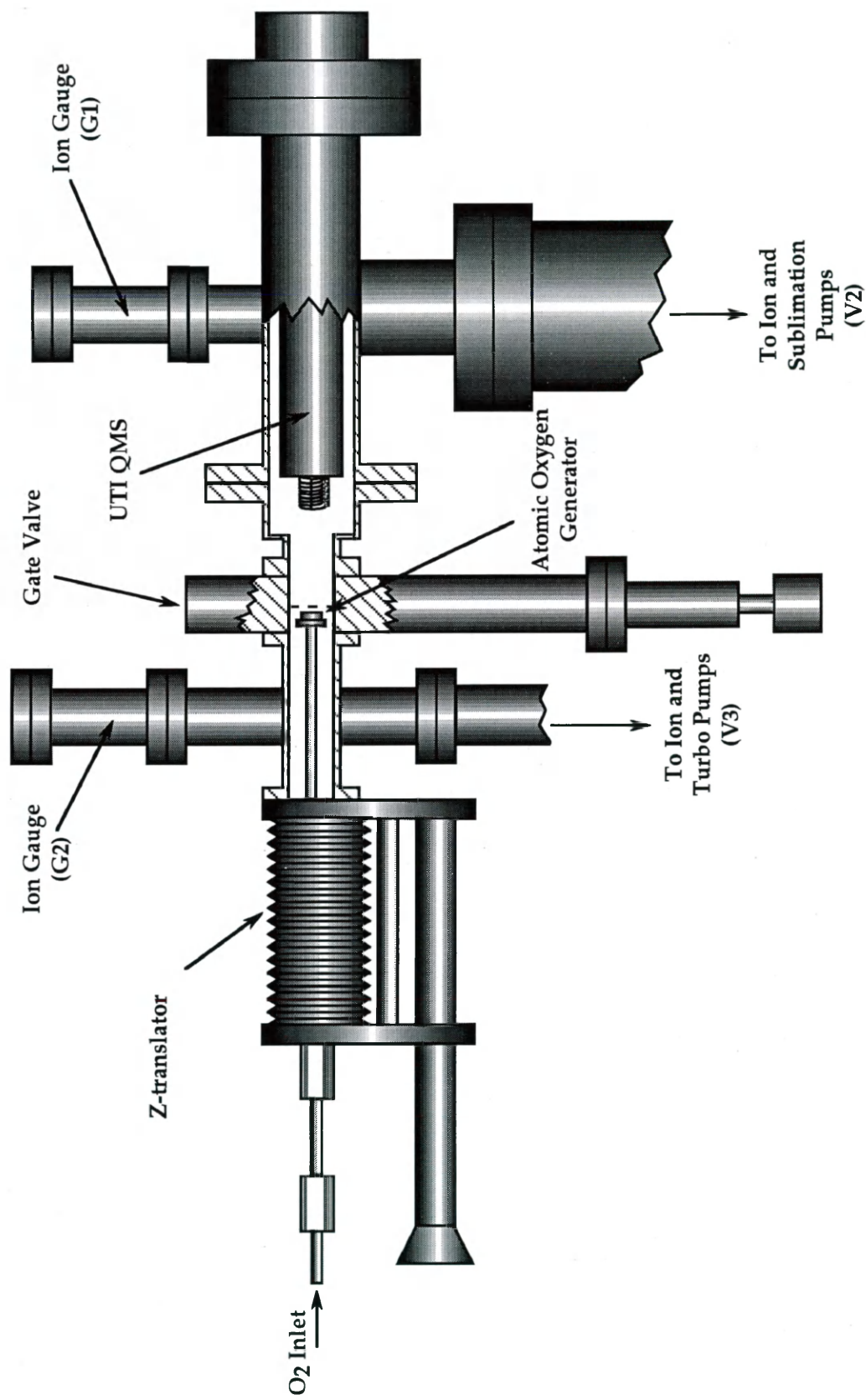


Figure 12. The calibrated ion gauge (standard gauge) was placed in the system behind the ion gauge (G1) in the detection chamber side of the system. Valve (V1) connected the standard gauge to a turbo pump located on the other side (in the plane of the paper) of the detection chamber ion pump.

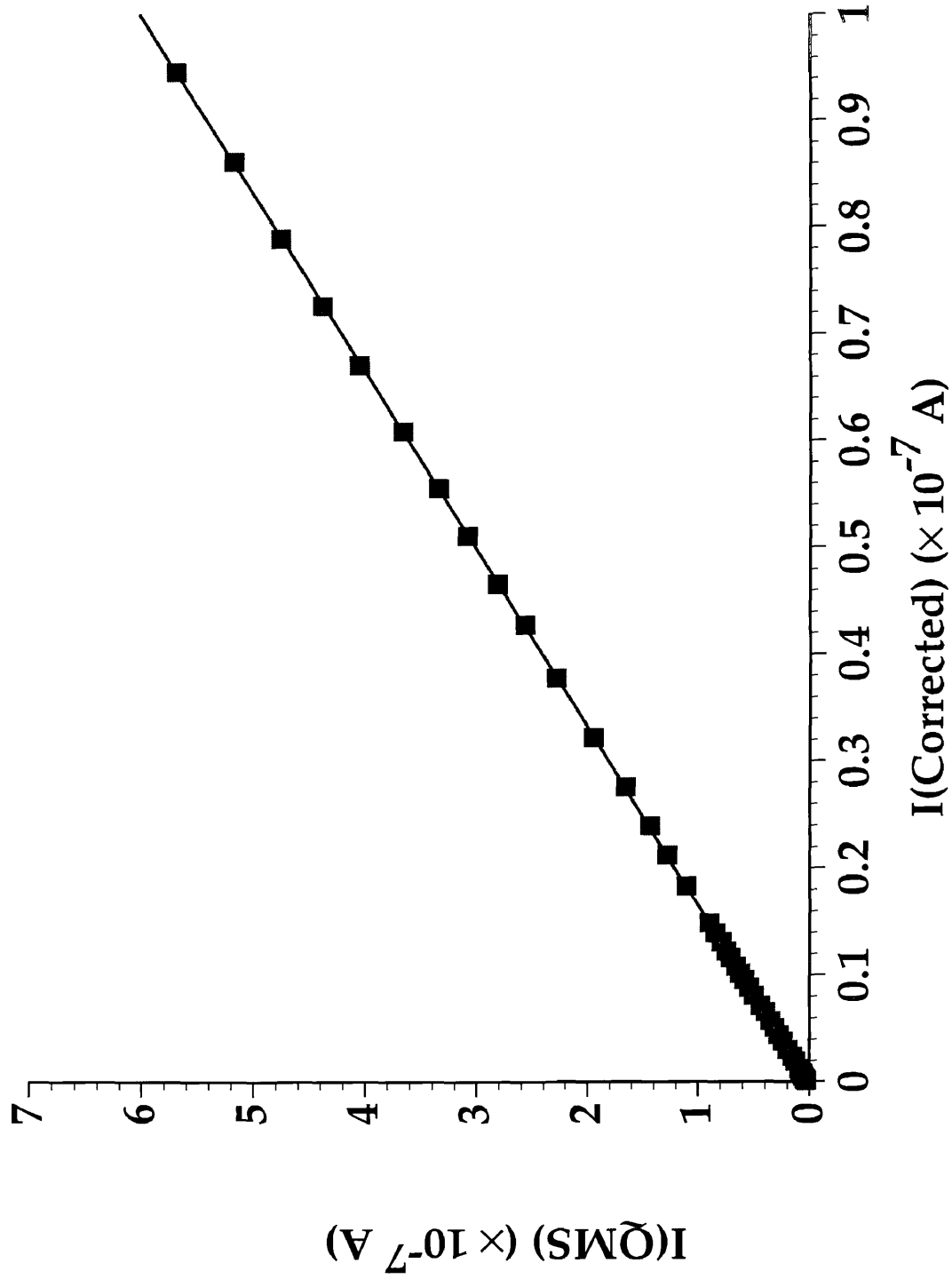


Figure 13. Plot of the I(G1 corrected) vs. I(QMS) used to calibrate mass spectrometer for O flux determination.

$$\frac{\sigma_O}{\sigma_{O_2}} = \left(\frac{E_{O_2}}{E_O} \right)^2, \quad (3)$$

where σ is the cross-section and E is the ionization potential (13.55 eV for O and 12.5 eV for O₂).¹⁰ Since the ion currents detected by the QMS are proportional to the cross-section, with the known ionization potentials and the calibrated sensitivity for QMS to O₂, then the ratio of the sensitivity of atomic oxygen to molecular oxygen can be calculated:

$$\frac{S_O}{S_{O_2}} = \left(\frac{E_{O_2}}{E_O} \right)^2 = 0.85. \quad (4)$$

This value is used in the oxygen flux calculation in the following section.

CHAPTER III

EXPERIMENTAL PROCEDURES

A. OXYGEN FLUX CALCULATION

The atomic oxygen flux can be calculated from the ionizer efficiency which is the ratio of the oxygen atom ion flux exiting the ionizer (J_{out}) to the oxygen atom flux entering the ionizer (J_{in}) and was determined, for this QMS, from:⁸

$$\frac{J_{out}}{J_{in}} = \frac{S_O k_B T}{A e v_{in}}, \quad (5)$$

where S_O is the QMS sensitivity for O, 8.59×10^{-3} A/Torr at 0.2 mA emission current and RIEM mode; k_B is Boltzmann's constant, 1.38×10^{-23} J/K; T is the gas temperature (K), A is the area of the aperture, 0.508 cm^2 ; e is the electronic charge, 1.6×10^{-19} C; and v_{in} is the velocity of the entering particles, $7.7 \times 10^5 \text{ cm s}^{-1}$. The velocity of the O neutrals was assumed to be the same as O^+ , which was previously measured.

B. MODES OF OPERATION

In the UTI mass spectrometer normal operation, the mass species were scanned from 1 to 50 mass/charge units, the ionizer voltage was set at 15 V ion energy, the electron energy was set at 70 V, and the extraction voltage was set at -20 V. In this mode, all species in the system were ionized and detected.

Within the normal operation of a mass spectrometer, the pressure is an important consideration for determining the optimum emission current, peak height, and resolution.¹¹ The peak height is a function of the emission current. Typically for operating pressures $> 5 \times 10^{-6}$ Torr, the emission current is kept between 0.6 and 0.8 mA. In this region, a change in the emission current produces a linear change in the peak height (figure 14a). For pressures $< 5 \times 10^{-6}$ Torr, the emission current can be set between 2 and 4 mA with small changes in peak height (figure 14b). In this region, the change is nonlinear. Also, as the emission current increases, the electron density in the center region of the ion grid increases. At the higher emission currents, the electron space charge effects becomes dominant and substantially increases the probability of ionization and, therefore, the sensitivity. Space charge however, may cause fluky, non-reproducible results. Even though the operating pressures of this experiment were $< 10^{-7}$ Torr, because of these space charge effects, the emission current was kept in the linear range (0.5 mA).

The reduced ion energy mode (RIEM) is an operational mode that makes use of the directional energy of an ion. To operate in the RIEM, the extraction voltage was set at 0 V. With an extraction voltage of -20 V, ions that are extracted into the filter region have 15 V added to their existing directional energy. A minimum of 2 V is needed for a species to transit the filter region of the quadrupole and reach the detector. By setting the extraction voltage to 0 V, only those ions with more than 2 V of directional energy can reach the detector. Species with less than 2 eV are filtered out by the quadrupole rods. Of the species present in the system: C, CO, CO₂, O, and O₂, only atomic oxygen has a directional energy > 2 eV. Because of the ESD

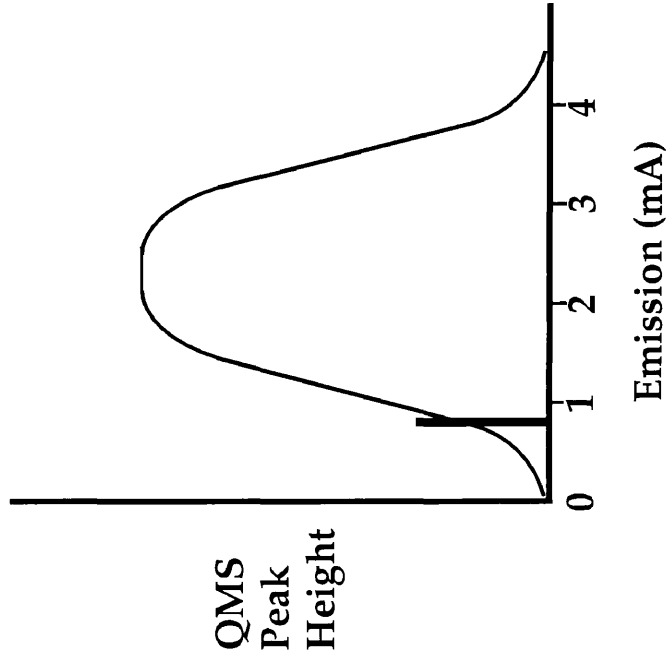


Figure 14.a. The optimum emission for high pressure operation ($>5 \times 10^{-6}$ Torr) is between 0.6 and 0.8 mA. Small changes in emission current can have a large effect on peak height.

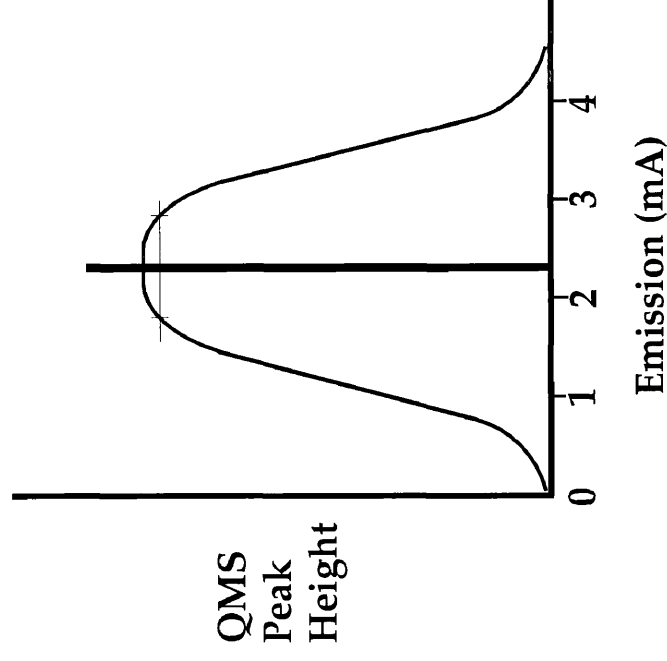


Figure 14.b. Peak height is a function of emission current. For low pressures ($<5 \times 10^{-6}$ Torr), the desired operating emission is between 2 and 4 mA where a small change in emission current has little effect on peak height.

mechanism, atomic oxygen is hyper-energetic¹² with a directional energy around 5 eV and is the only species to be able transit the filter region in the RIEM. The RIEM operation permits the enhancement of the atomic oxygen signal.

The appearance potential mode (AP) is a method to separate species by their ionization potential. The electron energy within the grid can be decreased so that only species below a certain ionization potential will be ionized and eventually be detected. The electron energy is the potential difference between the grid voltage and the filament voltage. The filament is typically operated at -55 V and the grid at +15 V, giving the electrons 70 eV potential energy. Of the major species present, atomic oxygen and molecular oxygen have lower first ionization potential (13.6 and 12.5 eV respectively) than CO and CO₂ (14.1 and 14.4 eV respectively). Table 2 lists the first ionization potential of the species present in this experiment.

Table 2
First Ionization Potential of Selected Species¹⁰

CO	14.1 V
CO ₂	14.4 V
H ₂ O	12.56 V
O	13.55 V
O ₂	12.5 V

By lowering the grid voltage to 7.5 V and the filament voltage to 9 V (selected because of an electronic control unit limit), the energy of the electrons (work function) would be 13.8 V which would be sufficient to ionize O, O₂, and H₂O, but not CO and CO₂.

Although, O₂ and H₂O are still ionized, the concentrations of these species are sufficiently low that their presence does not interfere with the detection of atomic oxygen.

In order to observe the behavior of the reaction products as well as the atomic oxygen, the majority of this research was conducted in a modified RIEM where the grid voltage was 7.5 eV. The ion energies entering the QMS filter are therefore 7.5 eV.

CHAPTER IV

RESULTS

Figure 15a shows the normal mode spectrum of the UTI quadrupole mass spectrometer when the oxygen generator is operated at 400 Torr O₂ upstream pressure, an ESD voltage of 1.0 kV and an ESD current of 5 mA. The CO and CO₂ signals are clearly dominant and represent a high concentration of system surface carbon that readily combines with the scattered atomic oxygen. Figure 15b shows the same set of conditions in the reduced ion energy mode (RIEM) when the grid potential of the QMS is reduced to 7.5 eV. The sensitivity of all species is reduced, but the more energetic oxygen atoms ($m/e = 16$) are less impacted by the ionizing energy and exhibit a prominent signal. It is not desirable to completely shut off the reaction products because they are also of interest, so the RIEM mode was primarily used in this study. There are several aspects of this result that will be discussed later.

The variation of atomic oxygen as the ESD voltage is cycled on and off is shown in figure 16. The structure at the top of these ESD "on" regions can be simply explained. Initially, when the ESD voltage is first applied, the oxygen surface coverage is higher, giving rise to a larger flux, but then decays to some steady state level. When the ESD voltage is turned off, the signal immediately drops to some baseline level associated with the fragmentation of oxygen bearing species.

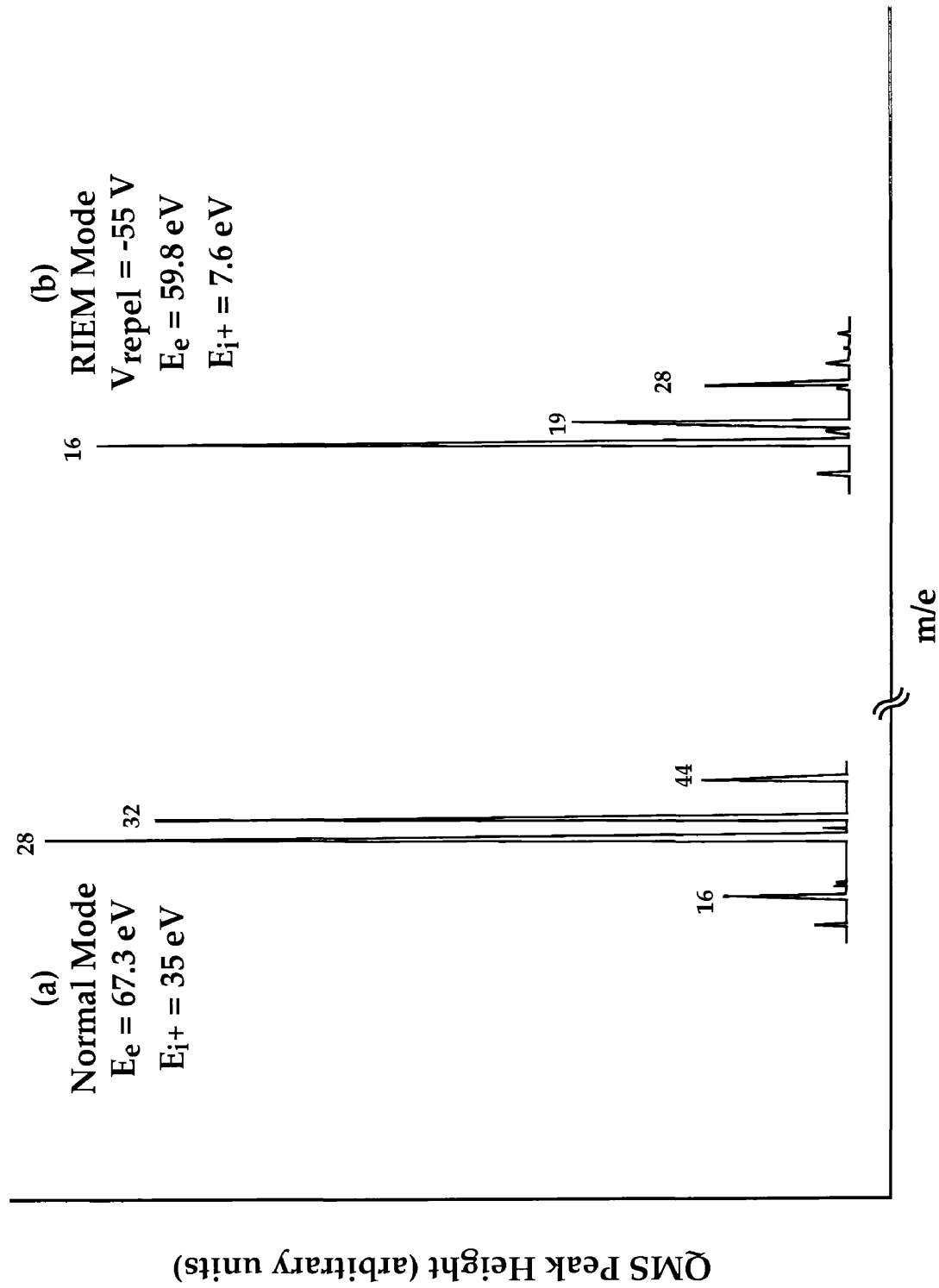


Figure 15. Mass spectra of normal mode (a) and the reduced ion energy mode (b) of atomic oxygen and the reaction products.

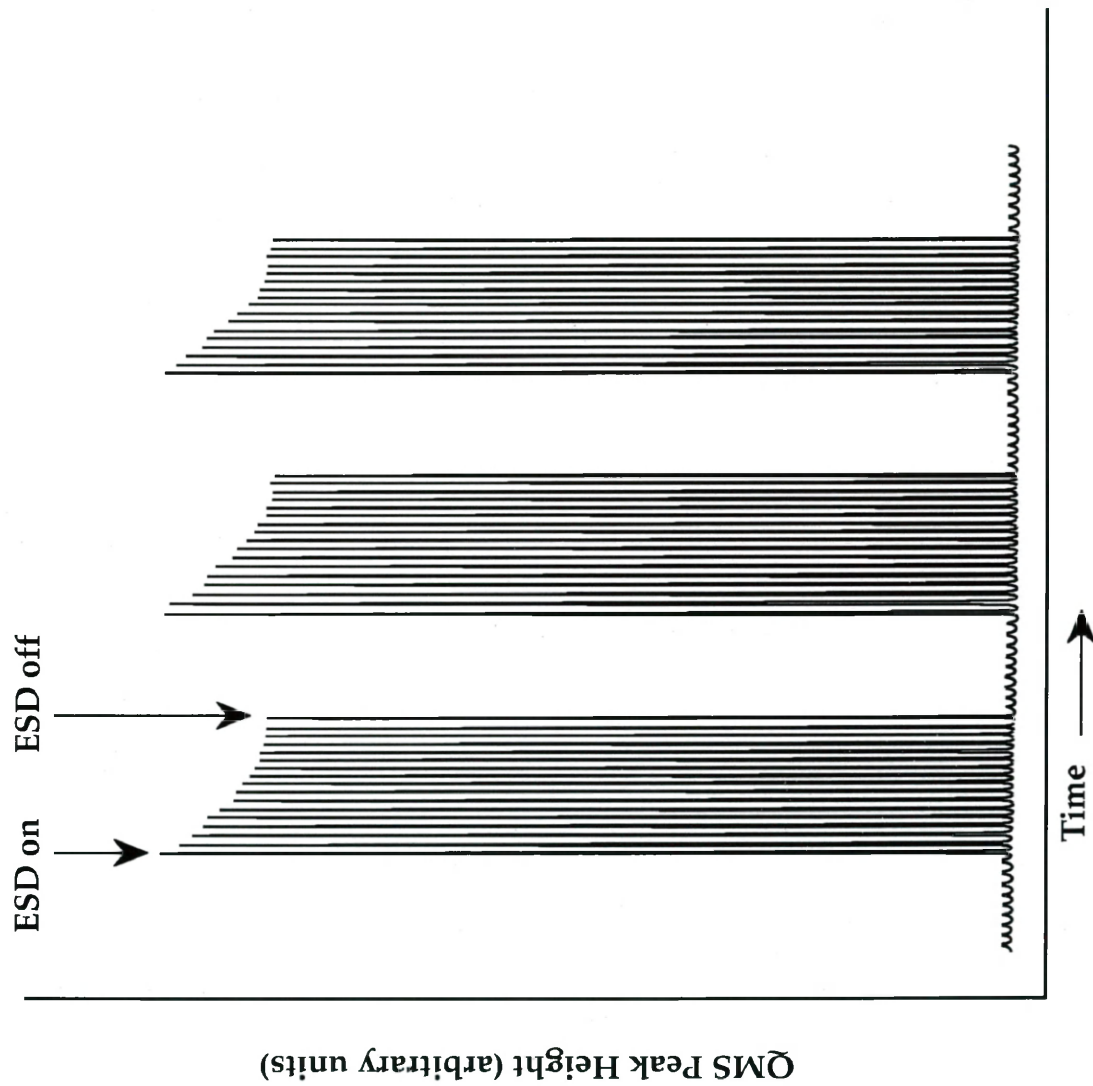


Figure 16. The variation of atomic oxygen ($m/e = 16$) as the ESD current is cycled on and off. $T = 375^\circ \text{C}$; $V_{\text{ESD}} = 400 \text{ V}$; $I_{\text{ESD}} = 4 \text{ mA}$.

Figure 17 represents the variation in species as a function of ESD current. At low levels of bombardment (< 1 mA) the O_2 was more than half that of steady state permeation, but as the ESD current was increased the molecular oxygen decreased to less than 15% of the permeation level (10 mA). Simultaneously, the atomic oxygen increased with the expected linearity. This was also observed with the reaction products such as CO. A logical explanation for this is that some of the oxygen emerging at the surface is desorbed by ESD before it has time to surface diffuse and recombine to form O_2 . The higher the ESD current the more the fraction of available surface O is desorbed.

A plot of detected flux versus ESD current for a family of voltages is shown in figure 18. The highest flux detected by the QMS was 1×10^{13} atoms $cm^{-2} s^{-1}$ at 400 eV and 375 ° C membrane temperature. Although the curves are not strictly linear, it is clear that at the higher electron energies, the more linear they are. Past experiments using a separate electron gun have shown strict linearity with ESD currents to the slight non-linearity observed here may be because of the effect of field distortion from the proximity of the chamber walls and the isolation valve. Figure 19 shows the atomic oxygen flux as a function of electron energy for a constant ESD current of 8 mA. With this design, the lens currents at an ESD voltage of 200 V were too high for good focusing. It does appear, however, that low voltage design would be desirable.

The flux increase with membrane temperature for 1200 V ESD voltage and for 2 mA ESD current is shown in figure 20. An Arrhenius plot extending from 300 to 500° C is linear up to 475° C where the oxygen surface

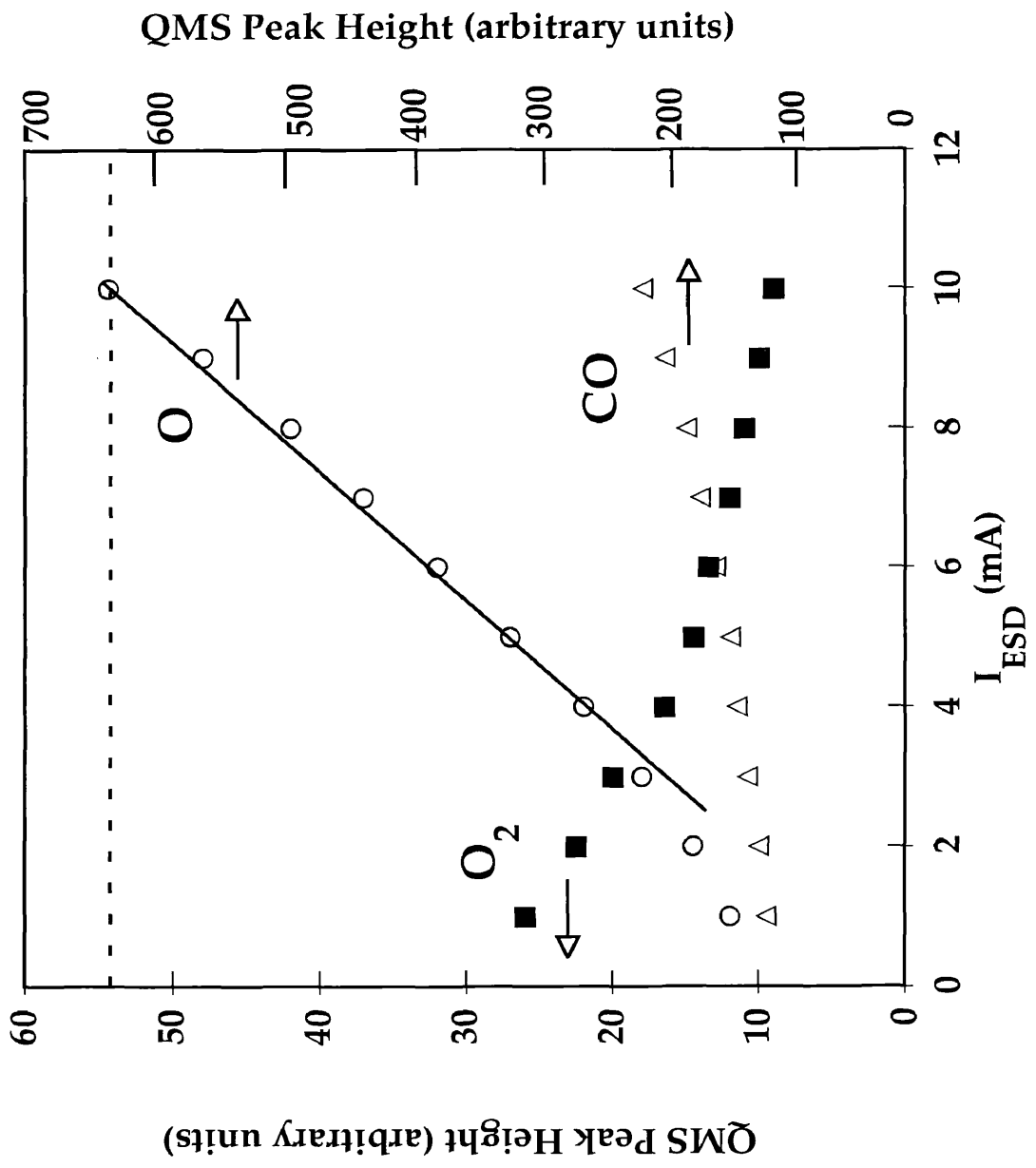


Figure 17. The variation in the species as a function of ESD current is illustrated in this graph.

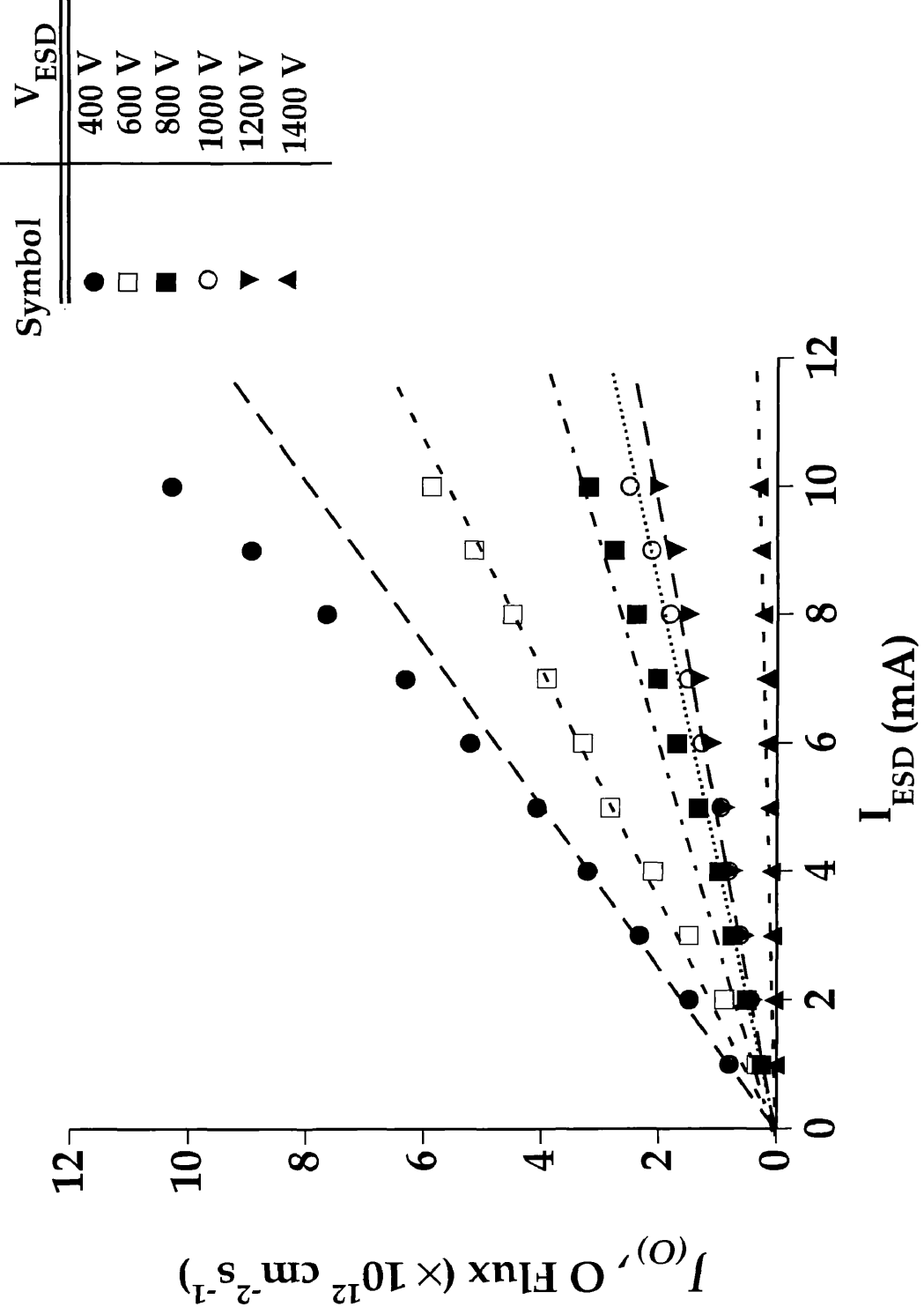


Figure 18. The detected flux vs. ESD current for a family of voltages is shown in this graph.

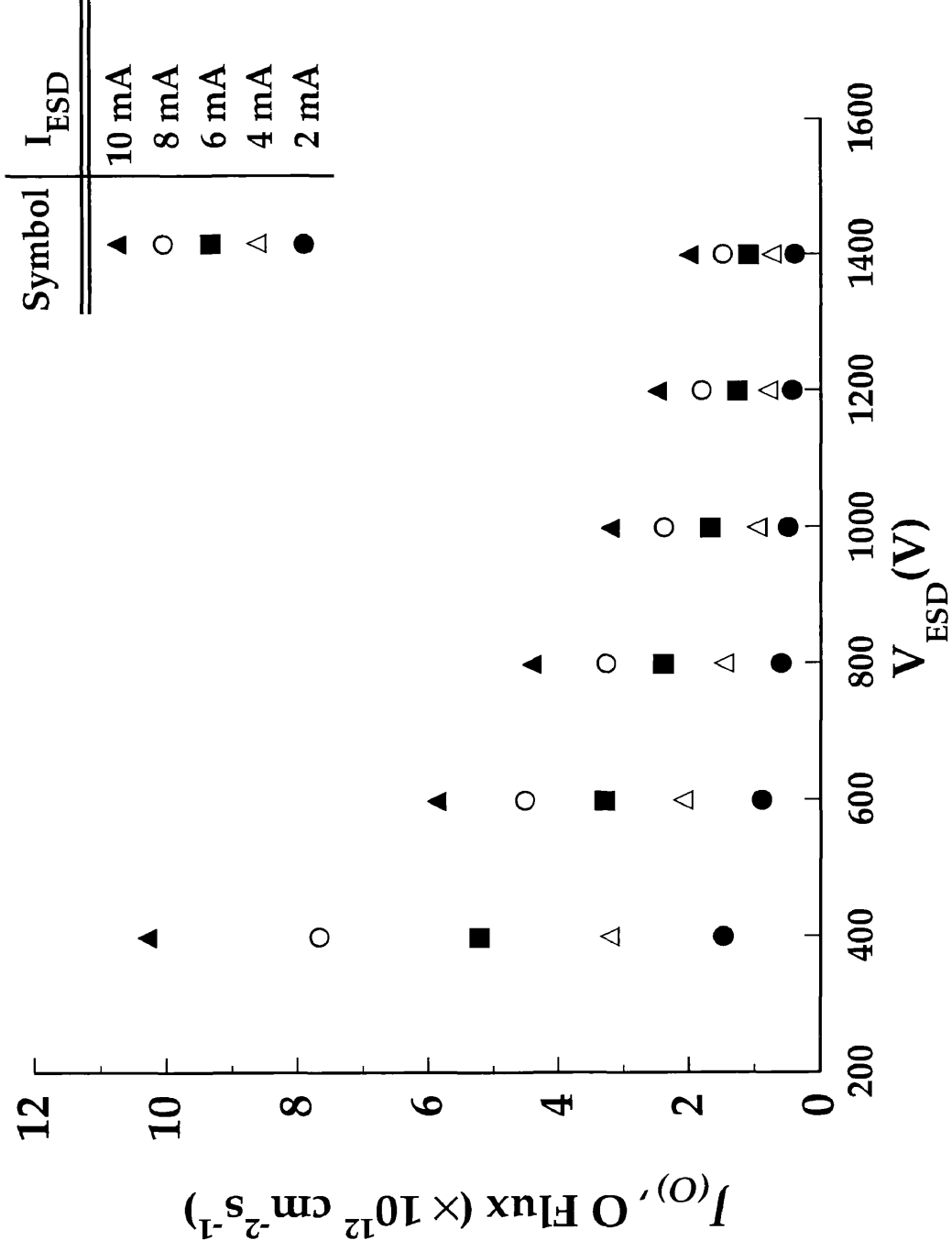


Figure 19. The atomic oxygen flux as a function of electron energy for a constant ESD of 8 mA.

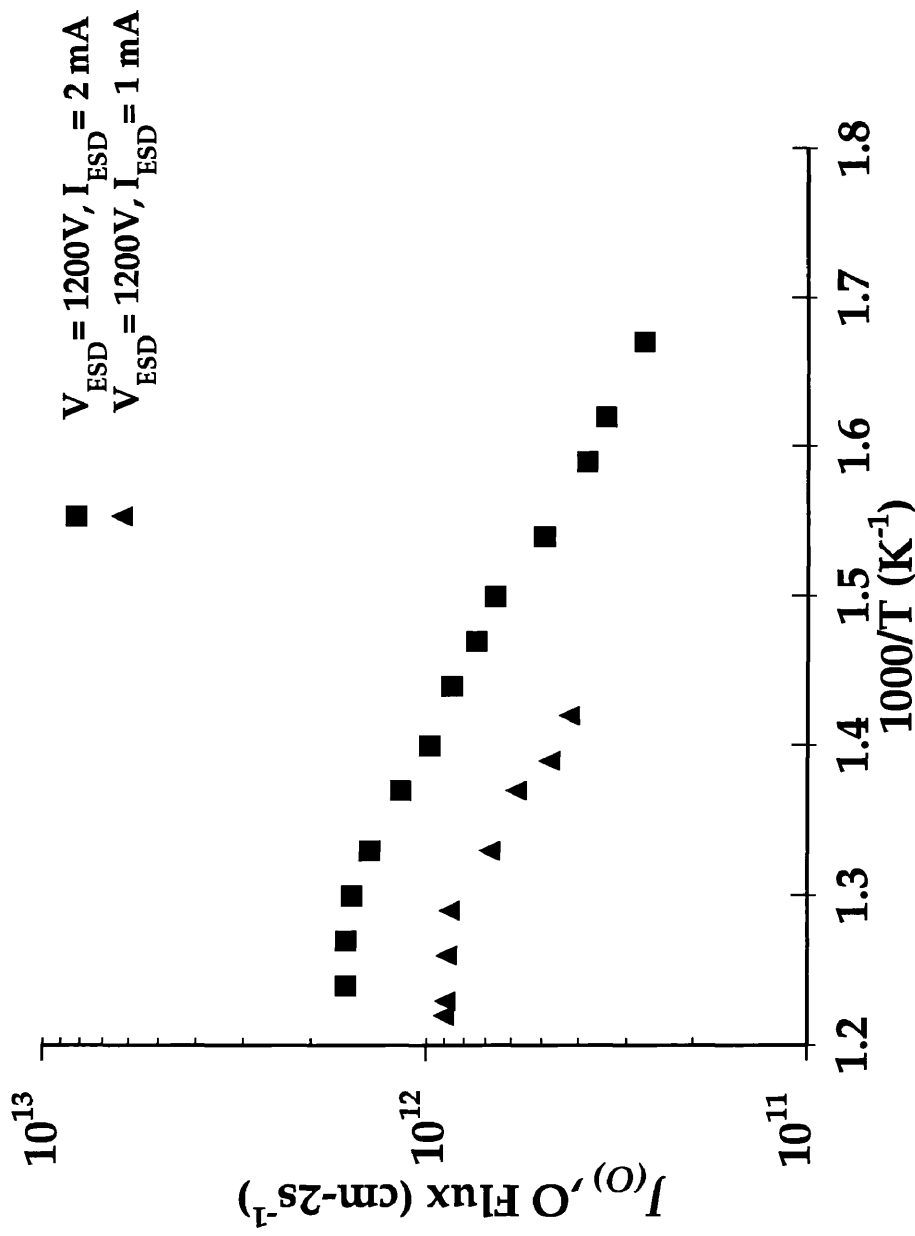


Figure 20. An Arrhenius plot from 300-500° C.

concentration at the UHV interface becomes a constant and no longer increases with temperature. Further, the ESD yield scales with bombardment current which is consistent with observed theory. The activation energy for the linear portion was found to be 14.4 kcal/mole which compares with the 22.7 kcal/mole measured for ordinary molecular dissociative permeation.³ This suggests that there is a UHV membrane side surface limitation in ordinary permeation which has a significant effect within this temperature range. Bombardment with electrons substantially enhances the desorption process.

A measure of the cross-section at different ESD currents is presented in figure 21. The temperature of the membrane was charged at 400° C and then reduced to 100° C to insure a minimum of oxygen transport so that there is no resupply of the surface. In this way, the signal decay as a function of time method for determining the cross-section could be utilized. Calculation of the cross-section at 0.5, 1, 2, and 5 mA gave $\Omega = 4.5 \times 10^{-18} \text{ cm}^2$ consistently for all the ESD currents studied. This value is considerably higher precision than past estimates in that the parameters are more accurately known. The variable with most uncertainty in the calculation is the surface coverage but that can be reasonably approximated from a Fick's 1st law estimate.

Figure 22 is a plot of the oxygen flux as a function of the detector distance from the source for a \cos^n distribution. The solid diamonds represent the theoretical values for the oxygen flux measured as the relative ion intensity of the atomic oxygen along the z-axis. The calculated flux for $\cos \alpha$, $\cos^2 \alpha$, and $\cos^3 \alpha$ distributions along the z-axis were indistinguishable from each other when plotted and were within noise levels for experimental

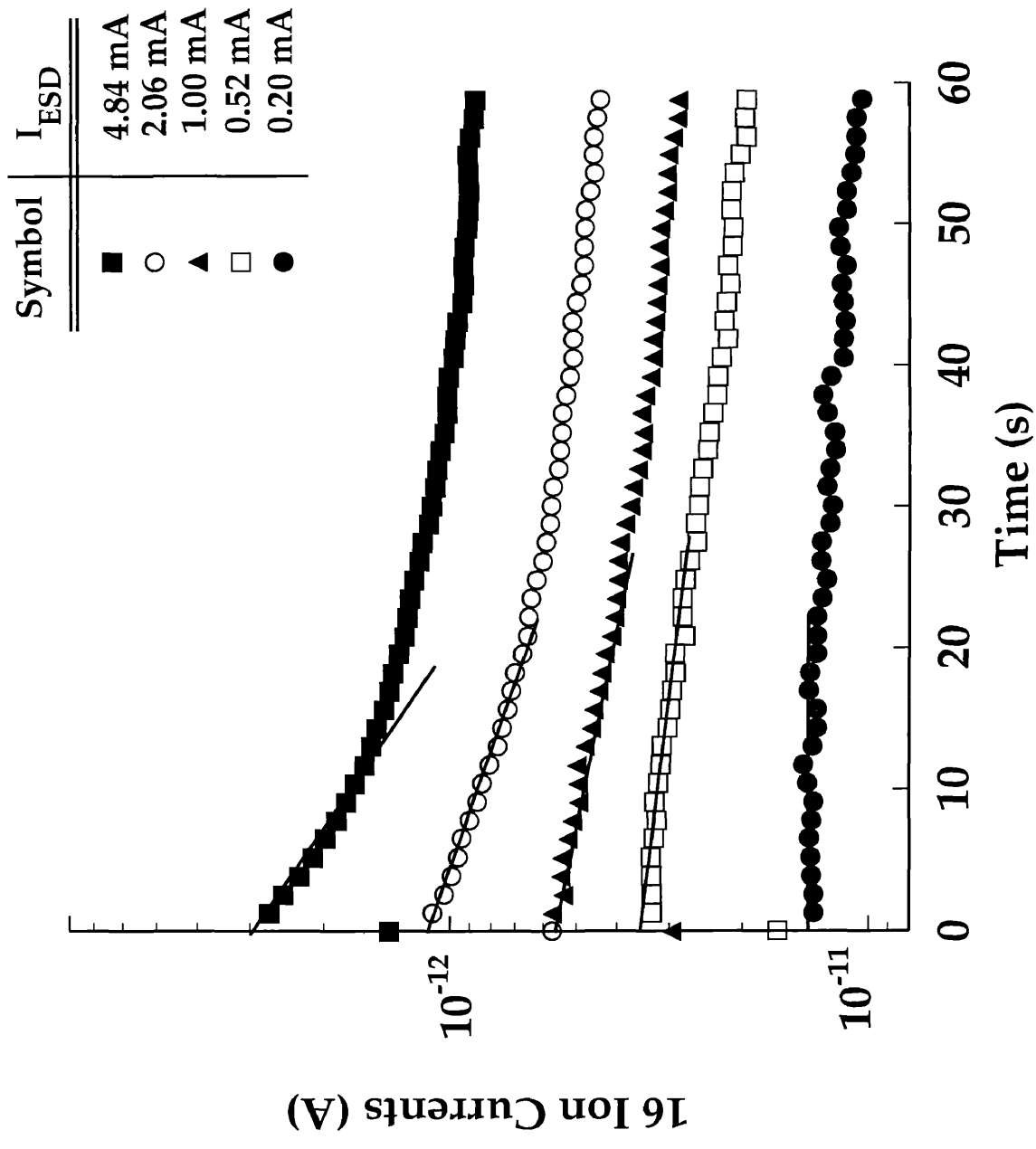


Figure 21. A measure of the cross-section at different ESD currents.

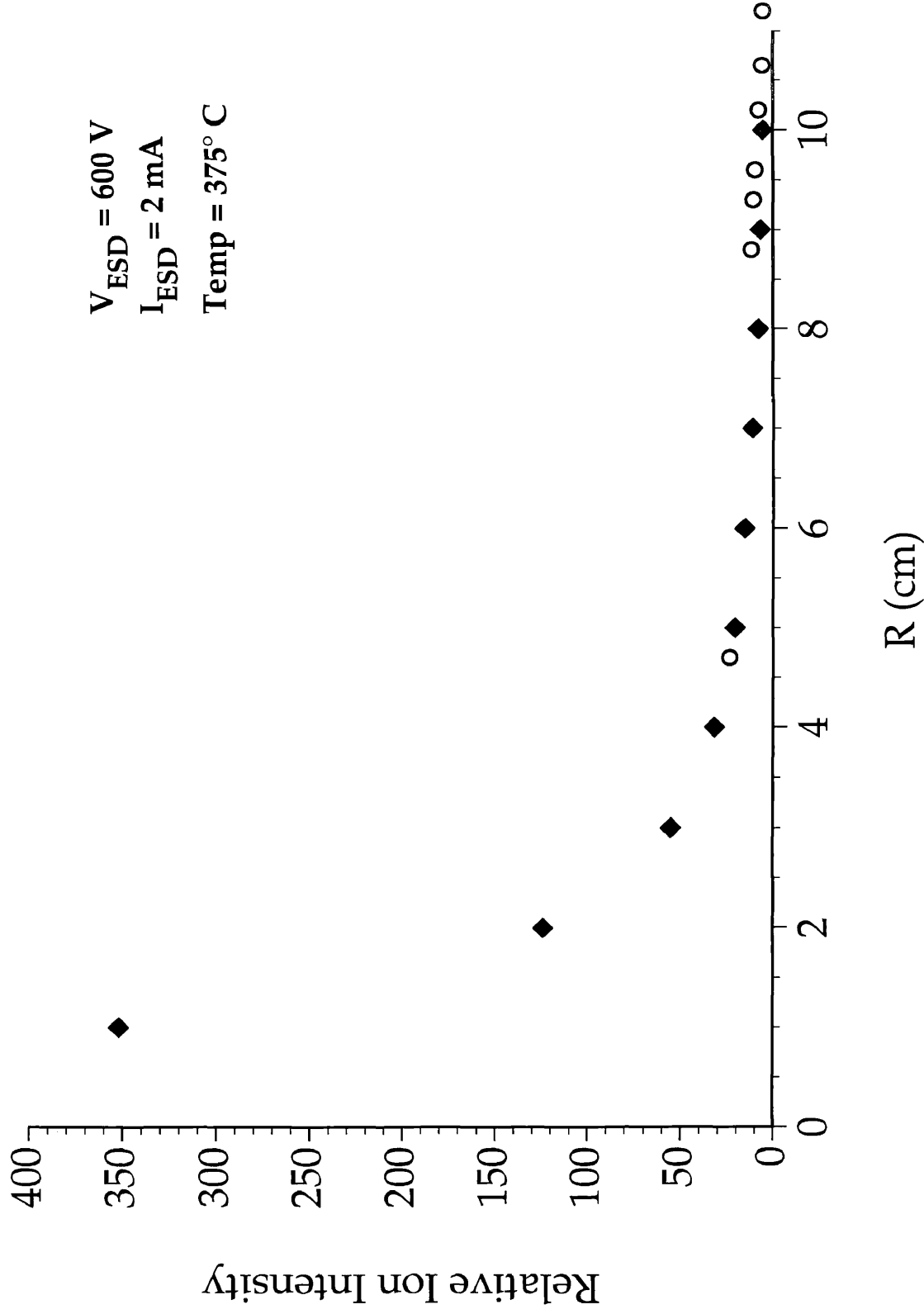


Figure 22. The curve represented by the solid diamonds is a plot of $\cos \alpha$, $\cos^2 \alpha$, and $\cos^3 \alpha$. The curves for each fall on top of each other. The open circles represent the experimental values.

values. Any determination of the flux as a function of the distance from the detector along the z-axis was not possible.

The open circles represent the experimental flux values. These points fall along the curve indicating that the flux distribution is generally followed, but this approach was not going to allow a determination of n .

CHAPTER V

DISCUSSION

A. FLUX MEASUREMENTS

Figure 19 clearly shows that the magnitude of the flux increases with decreasing voltage. If the instrument is operated at an ESD voltage of 400 V, and ESD current of 10 mA, an upstream pressure of 400 Torr (O_2) and a membrane temperature of 500° C, the flux measured at the QMS was approximately 5×10^{13} atoms $cm^{-2} s^{-1}$. When the ESD electron energy was reduced to 200 eV, the flux increased a factor of 2, but the lens current was so high that a significant ESD generated CO signal from adsorbed CO on the stainless steel occurred, somewhat contaminating the O flux.

It is interesting to note the variation in O_2 and the reaction products such as CO as a function of ESD current. Figure 17 is a plot of the major species in the RIEM mode. The declining O_2 is essentially the result of competing rates of recombination of atomic oxygen from the ESD of adsorbed atoms and the surface diffusion of the species colliding on the surface, recombining and desorbing as O_2 . The higher the ESD current the greater the quantity of O desorbed and the less surface oxygen available for O_2 desorption. Further, as a result of the higher atom flux, there is more association to CO and CO_2 . The dashed line in the figure is the steady state permeation at a membrane temperature of 375° C and an upstream pressure of 400 Torr (O_2).

It represents the maximum recombination to O₂ possible for the indicated conditions.

B. PERMEATION LIMITATIONS

The Arrhenius plot of the atomic oxygen flux at 1 mA and 2 mA (1.2 kV electron energy) shows linearity over the temperature range 300-475° C. Above that temperature, the flux becomes a constant for the indicated ESD current. The linearity is an indication of diffusion controlled kinetics and suggests that the surface concentration of oxygen atoms at the UHV interface is a steady state value less than for ordinary permeation. For example, figure 20 shows the atomic oxygen (top of the square wave) decay in the flux from the initial level (steady state permeation) to the steady state level (permeation less ESD desorption). A change in the ESD current gives the expected proportional change in flux. The constant flux level at temperatures above ~ 475° C indicates that the surface concentration available to ESD is unchanging. Beyond this point, any increase in temperature results in only increased O₂ desorption. The net surface concentration available to ESD at this point is unchanging. Accordingly, the ESD yield scales proportionally with bombardment current, in that the magnitude increased by a factor of 2 between 1 and 2 mA. The activation energy suggests for the linear portion of the curves was found to be 14.4 kcal/mole, which can be compared with the 22.7 kcal/mole measured for ordinary oxygen permeation. The lower activation energy suggests the ESD mechanism of desorption on the downstream surface is significant in reducing the overall sequence barriers to the transport of oxygen.

C. O/Ag (poly) ESD CROSS-SECTION

Measurement of the ESD cross section was achieved in the conventional way using the QMS signal decay as a function of time. The membrane was charged at 400° C without ESD and reduced to ~ 100° C to minimize the diffusional transport or supply of oxygen to the surface. The ESD was initiated and the flux decay monitored as a function of time. Experiments were run at 0.5, 1, 2, and 5 mA of ESD current. The results of this decay are shown in figure 21. The initial slope was used for calculation of the cross section. The standard decay as a function of time method for determining the cross-section (Ω) can be calculated from:⁸

$$\Omega = -\frac{Ae}{I_e t} \ln\left(\frac{i}{i_0}\right). \quad (6)$$

where i is ion current at time t , i_0 is the initial ion current at $t = 0$, I_e is ESD current, and A is the surface area.

The results are self consistent and give a value of $\Omega = 4.5 \times 10^{-18}$ cm². A comparison to other atom species desorbed by ESD shows this magnitude to be large, but well within the range for other systems.¹³ Previous measures of oxygen from Ag were found to be as high as 9×10^{-19} cm².¹² This value was based on a single crystal Ag (110) concentration of 6.5×10^{14} cm⁻² when it was for a polycrystalline wire. The results indicate surface coverage to be a factor of 4 larger; so the present results would be in good agreement with the corrected values of the previous work. Using this value of the cross section and the flux level detected for a membrane temperature of 375°C, an upstream pressure of 400 Torr O₂, an emission current of 8 mA and a ESD

energy of 400 eV, we found that the surface concentration at the downstream surface is $7.4 \times 10^{12} \text{ cm}^{-2}$ by eq. (24). This is almost two decades lower than what was measured for equilibrium coverage on Ag (110) single crystal ($6 \times 10^{14} \text{ cm}^{-2}$) without ESD.⁵ According to Fick's law, the significantly reduced surface concentration at the downstream side of the membrane increases the concentration differential across the membrane as well as the oxygen permeation through the membrane. The combined effects of the ESD and the increased permeation result in an increase in the atomic oxygen flux compared to the oxygen permeation without ESD.

CHAPTER VI

CONCLUSIONS

The emission characteristics of atomic oxygen generated by electron stimulated desorption (ESD) from the downstream surface of polycrystalline Ag membrane were studied. It was found that the flux levels of atomic oxygen were approximately linear with electron bombardment current and measured up to approximately $1 \times 10^{14} \text{ cm}^{-2} \text{ s}^{-1}$ (electron bombardment flux at 10 mA cm^{-2} at 375 V) at the emission plane. An Arrhenius plot of the flux showed linearity up to 475° C where the surface concentration for oxygen adatoms became constant. The cross section for the ESD process was determined at different emission currents and found to be $4.5 \times 10^{-18} \text{ cm}^2$.

The experimental design employed was not suitable for determining the spatial distribution of the oxygen flux; however, the experimental values did fall on a \cos^n plot. Future experiments should look at flux distributions off the x-axis.

The instrument itself turned out not to be user friendly. This system can work in a research environment, but requires a lot of pampering and patience. It was designed to be used in a UHV environment and can be easily installed into an existing system. However, the instrument requires about two weeks of operating and clean-up before meaningful data can be obtained.

However, with great care, this instrument should be able to achieve the initial goal of producing a pure beam of ground state atomic oxygen with a

mean ion energy of 5 eV suitable for performing cross-beam experiments. In addition, it is the only instrument suitable for UHV environments.

REFERENCES

1. S. L. Koontz, K. Albyn, and L. J. Leger. *J. Spacecraft* , **28** (1991) 315.
2. L. J. Leger, I. K. Spiker, J. F. Kuminecz, T. J. Ballentine, and J. T. Visentine, AIAA Paper 8-2631 (November 1983).
3. L. J. Leger, J. T. Visentine and J. F. Kunminecz, AIAA Paper 84-0548 (January 1984).
4. W. Eichenauer and G. Müller, *Z. Metallkd.* **48**, (1962) 321.
5. R. A. Outlaw, G. B. Hoflund, and G. R. Corallo, *Applied Surface Science*, **28**, (1987) 235-246.
6. N. H. Tolk, M. M. Traum, J. C. Tully, T. E. Madey, *Desorption Induced Electronic Transitions*, Springer Verlag, Berlin (1982) 46.
7. R. A. Outlaw, W. K. Peregoy, G. B. Hoflund, and G. R. Corallo, *Electron Stimulated Desorption of Atomic Oxygen From Silver*, NASA TP-2668, April 1987.
8. R. A. Outlaw and M. R. Davidson, *J. Vac. Sci. Technol. A* , **12** (3) (May/June 1994) 1-7.
9. J. B. Hasted, *Physics of Atomic Collisions*, 2nd Ed., Butterworth & Co., Ltd.; London (1972) 388.
10. *CRC Handbook of Chemistry and Physics.*, 70th Ed., Robert C. Weast, David R. Lide, Melvin J. Astle, and William H. Beyer, Ed., CRC Press, Inc., Boca Raton, FL (1989) E-80 - E-91.
11. UTI Model # 100C Quadrupole Mass Analyzer Operation Manual (Uthe Technology International) Appendix A.
12. T. E. Madey and J. T. Yates, Jr., *Surf. Sci.* **63** (1977) 2093.
13. T. E. Madey and J. T. Yates, Jr., "Electron Stimulated Desorption as a Tool for Studies of Chemisorption," *J. Vac. Soc. Techol.* **8** (1971) 525.

REFERENCES (Continued)

14. Bruce A. Banks and Sharon K. Rutledge, "Low Earth Orbital Atomic Oxygen Simulation for Materials Durability Evaluation," Proceedings from the Fourth International Conference of Spacecraft Materials in Space Environment, Sept. 6-9, 1988, CERT, Toulouse, France; pp 371-392.
15. N. R. Lerner and T. Wydeven, *J. Electrochem. Soc.*, **136** (May 1989) 1426-1430.
16. B. Singh, L. J. Amore, W. Saylor, and G. Racette, *Laboratory Simulation of Low Earth Orbital Atomic Oxygen Interaction with Spacecraft Surfaces*, AIAA 23rd Aerospace Sciences Meeting, January 14-17, 1985/Reno, Nevada: AIAA-85-0477.
17. O. J. Orient , A. Chutjian, E. Murad, *Physical Review A*, **41** (7) (1990) 4106-4108.
18. J. B. Cross, L. H. Spangler, M. A. Hoffbauer, and F. A. Archuleta. "High Intensity 5 eV CW Laser Sustained O-Atom Exposure Facility For Material Degradation Studies," *SAMPE Quarterly*, **18** (2) (January 1987) 41-47.
19. O. J. Orient, A. Chutjian, and E. Murad, *Physical Review Letters*. **65** (19) (Nov. 1990) 2359-2361.
20. G. E. Caledonia, R. H. Krech, B. L. Upschulte, D. M. Sonnenfroh, D. B. Oakes, and K. W. Holtzclaw, *Fast Oxygen Atom Facility for Studies Related to Low Earth Orbit Activities*, AIAA 17th Aerospace Ground Testing Conference, July 6-8, 1992/Nashville, TN: AIAA-92-3974.
21. H. W. Dursch and H. G. Pippin, "Effects of Simulated Environments on Properties of Selected Material," *Materials Degradation in Low Earth Orbit (LEO)*, Proceedings of the 119th Annual Meeting of the Minerals, Metals & Materials Society, Anaheim, CA (Feb. 17-22, 1990) 207-218.
22. T. G. Eck and R. W. Hoffman, *Study of Kapton Under Simulated Shuttle Environment*, NASA-CR-176003, NAG3-426, (July 1985).

REFERENCES (Continued)

23. D. E. Brinza, D. R. Coulter, R. H. Liang, and A. Gupta, "Production of Pulsed Atomic Oxygen Beams Via Laser Vaporization Methods," *Proceedings of the NASA Workshop on Atomic Oxygen Effects*, JPL Publication 87-14 (June 1, 1987).
24. M. McCargo, R. E. Dammann, J. C. Robinson, and R. J. Milligan, "Effects of Combined Ultraviolet and Oxygen Plasma Environment on Spacecraft Thermal Control Materials--Space Shuttle Payloads," *Proceedings from the Environmental and Thermal Control Systems For Space Vehicles*, Toulouse, France (Oct. 4-7, 1983).
25. J. B. Cross and N. C. Blais, "High Energy-Intensity Atomic Oxygen Beam Source," *Rarefied Gas Dynamics: Space-Related Studies*, Edited by: E. P. Munts, D. P. Weaver, and D. H. Campbell, Princeton Combustion Research Laboratories, Inc. Monmouth Junction, NJ (1988) 143-155.
26. G. W. Sjolander and L. E. Bareiss, "Martin Marietta Atomic Oxygen Beam Facility," *Proceedings from the 18th International SAMPE Technical Conference*, **18** (Oct. 7-9, 1986) 722-731.
27. L. L. Fewell, *J. App. Polymer Sci.* **41** (1990) 391-406.
28. S. L. Koonts, K. Albyn, and L. Lergger, *J. of the IES*, (March/April 1990) 50-59.
29. C. E. Batten, K. G. Brown, and B. W. Lewis, *A Spectral Study of Radio-Frequency Plasma-Generated Flux of Atomic Oxygen*, NASA TM-4612 (Dec. 1994).
30. D. C. Ferguson, *Laboratory Degradation of Kapton in Low Energy Oxygen Ion Beam*, AIAA Document A85-10675 (Nov. 83).
31. G. E. Caledonia, "Laboratory Simulations of Energetic Atom Interactions Occurring in Low Earth Orbit," *Rarefied Gas Dynamics: Space-Related Studies*, Edited by: E. P. Munts, D. P. Weaver, and D. H. Campbell, Princeton Combustion Research Laboratories, Inc. Monmouth Junction, NJ (1988) 129-142.

REFERENCES
(Continued)

32. J. A. Vaughn, R. C. Linton, M. R. Carruth, Jr., A. F. Whitaker, J. W. Cuthbertson, W. D. Langer, and R. W. Motley, "Characterization of a 5-eV Atomic Oxygen Facility," *Fourth Annual Workshop on Space Operations Applications and Research (SOAR '90)*, NASA Conf. Publication 3103, Vol. II (1991) 764-771.
33. R. C. Tennyson, *Canadian J. of Physics*, **69** (Aug.-Sept. 1991) 1190-1208.
34. J. J. Scialdone and C. H. Clatterbuck, *Fourth Space Application Material Coatings on the Long-Duration Exposure Flight (LDEF)*, NASA-TM-104574 (1992).
35. C. E. Gleit and W. D. Holland, *Analytical Chemistry*, **34** (11), (October 1962) 1454-1457.
36. Walter H. Kohl, *Handbook of Materials and Technologies for Vacuum Devices*, Reinhold Publishing Corporation; New York (1967) pp 475-485.
37. Private conversations with Dr. R. A. Outlaw.
38. H. Willard Hobart, Lynne L. Merritt, Jr. John, A. Dean, and Frank A. Settle, Jr.; *Instrumental Methods of Analysis*; D. Van Nostrand Company; New York City, NY; (1981) pp 565-605.

APPENDIX A

A SURVEY OF ATOMIC OXYGEN GENERATORS

A number of experimental instruments have been developed to produce intense sources of atomic oxygen in the energy range of 2 to 10 eV.¹⁴ Some of these include conventional techniques, such as plasma torches and microwave discharges that can produce oxygen atoms with kinetic energies of 0.1 to 1.0 eV and intensities of 10^{17} to 10^{19} atoms/S-sr.¹⁵⁻¹⁸ Other techniques include continuous optical discharge and pulsed laser breakdown.¹⁹⁻²⁰ A graphical figure of the available oxygen flux systems is shown in figure 1.¹⁴ The atomic oxygen experiments corresponding to figure 1 are listed in Table A-1.

Plasma torches form plasmas in helium by sustained DC arc discharge.¹⁸ A small amount of O₂ is injected downstream of the arc into the gas flow where it is thermally dissociated into oxygen atoms by the hot helium. The high temperature, followed by isentropic expansion through a nozzle, produces oxygen atoms in the range of 1-2 eV at intensities of 10^{18} to 10^{19} atoms/S-sr. Effusive sources, such as microwave discharges operated at low pressures and conventional plasma ashers where material samples are exposed outside the plasma glow, produce atomic oxygen beams of low energy and low intensity. If the oxygen atoms are expanded through a supersonic nozzle, the flux and energy can be improved. Likewise, seeding and/or

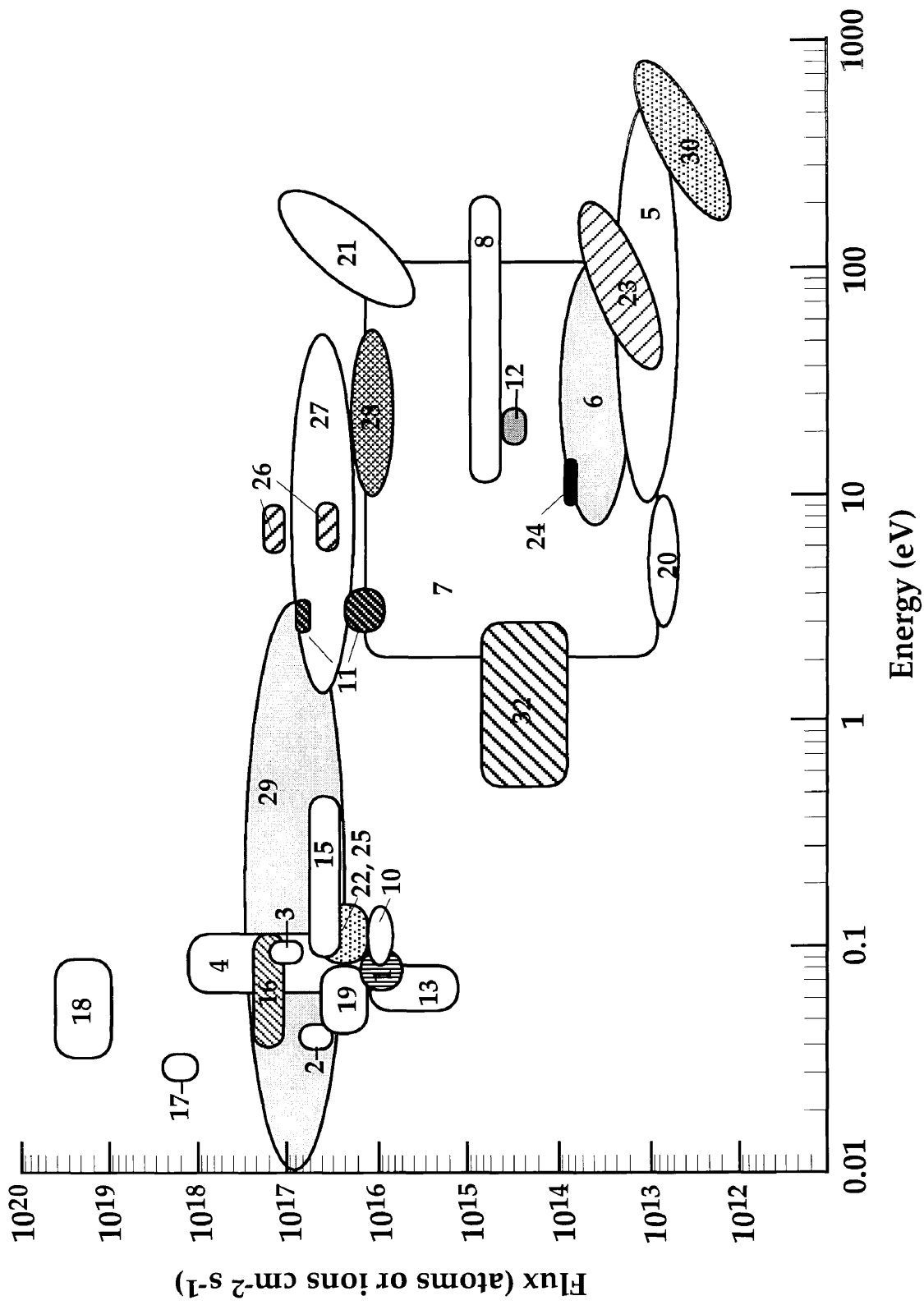


Figure A-1. A graphical illustration of the atomic oxygen test facilities showing the flux energy domains. 14

Table A-1
Atomic Oxygen Test Facilities¹⁴

Facility Number	Organization	Location	Facility Description	Test Program Participant
1.	University of Alabama	Huntsville, AL	Thermal A/O source	John Gregory
2.	Auburn University	Auburn, AL	RF plasma excited N is reacted with NO gas to produce thermal ground state A/O	Charles Neely
3.	Auburn University	Auburn, AL	RF plasma asher	Bruce Tatarchuk
4.	Boeing Aerospace Co.	Seattle, WA	Low frequency RF plasma; samples located downstream from glow	Gary Pippin ²¹ Roger Bourassa
5.	Case Western Reserve University	Cleveland, OH	Variable energy ion gun	T.G. Eck ²² Dick Hoffman
6.	David Sarnoff Research Center	Princeton, NJ	Single grid, low energy ion source	Bawa Singh ¹⁶
7.	General Electric- Space Division	Philadelphia, PA	Single grid ion source with charge exchange	Leo Amore James Lloyd
8.	Jet Propulsion Lab	Pasadena, CA	Formation of O ⁻ by dissociative attachment. Electrostatic acceleration of ions to final energy, then photo-detachment of electrons from ions with a laser	Ara Chutjian ^{17,19} Otto Orient
9.	Jet Propulsion Lab	Pasadena, CA	Pulsed laser induced breakdown followed by expansion through a nozzle	David Brinza ²³ Ranty Liang

Facility Number	Organization	Location	Facility Description	Test Program Participant
10.	Lockheed Palo Alto Research	Palo Alto, CA	RF plasma asher	Matt McCargo ²⁴
11.	Los Alamos National Laboratory	Los Alamos, NM	Continuous laser heated discharge	Jon B. Cross ^{18,25}
12.	Martin Marietta Denver Aerospace	Denver, Co	Ion gun; magnet for charge/mass selection; multi stage aperture for beam deceleration; deflection	Gary W. Sjolander ²⁶
13.	McDonnell Gouglass Aeronautics Co,	Huntington Beach, CA	RF plasma system with Faraday cage	Esther H. Lan
14.	NASA-Ames Research Center	Moffett Field, CA	Microwave discharge, multisample chamber	Larry I. Fewell ²⁷
15.	NASA-Ames Research Center	Moffett Field, CA	RF O ₂ plasma; samples downstream from plasma glow	Morton Golub Ted Wydevan ¹⁵
16.	NASA-Ames Research Center	Moffett Field, CA	RF plasma with sample downstream for glow; sample is UV shielded	Narcinda R. Lerner
17.	NASA-Johnson Space Center	Houston, TX	Flowing afterglow	Steven L Kootz ¹
18.	NASA -Johnson Space Center	Houston, TX	RF plasma asher	Steven L. Kootz ²⁸
19.	NASA-Langley Research Center	Hampton, VA	RF plasma asher	Carmen E. Batten ²⁹

Facility Number	Organization	Location	Facility Description	Test Program Participant
20.	NASA-Langley Research Center	Hampton, VA	Electron stimulated desorption from polycrystalline Ag	R. A. Outlaw ⁸
21.	NASA-Lewis Research Center	Cleveland, OH	Electron bombardment gridless ion source	Bruce A. Banks ¹⁴ Sharon K. Rutledge
22.	NASA- Lewis Research Center	Cleveland, OH	RF plasma asher run on air	Bruce A. Banks ¹⁴ Sharon K. Rutledge
23.	NASA-Lewis Research Center	Cleveland, OH	Dissociation and ionization in tunable microwave cavity followed by electrostatic acceleration	Dale C. Ferguson ³⁰
24.	NASA-Marshall Space Flight Center	Huntsville, AL	Electron bombardment ion source with electromagnetic charge/mass selection downstream, then deceleration with charge neutralization and deflection of non-neutralized ions	Jill Carhorl
25.	University of Nebraska	Lincoln, NE	RF plasma asher	John A. Woollam
26.	Physical Sciences, Inc.	Andover, MA	Pulsed laser induced breakdown followed by expansion through a nozzle	George Caledonia ³¹ Robert Krech

Facility Number	Organization	Location	Facility Description	Test Program Participant
27.	Princeton Plasma Physics Laboratory	Princeton, NJ	Neutralization of ions formed in plasma by biased plate	William Langer ³² S. A. Cohen D. M. Manos R. W. Motley M. Ono S. Paul D. Roberts H. Selberg
28.	University of Texas	Austin, TX	Ion beam with charge exchange	Dennis Kohl
29.	University of Toronto	Downsview, Ontario Canada	Microwave generated plasma. Noble gas carrier transports A/O through skimmer to produce high flux density	Rod. C. Tennyson ³³
30.	Vanderbilt University	Nashville, Tn	Ion gun. Wein filter for charge state selection; deceleration of ions through system of grids; grazing incidence impact with polished nickel surface to neutralize ions. Electrostatic deflection of non-neutralized ions.	Royal Albridge N. Tolk
31.	NASA-Goddard Space Flight Center	Greenbelt, MD	RF plasma asher	John J. Scialdone ³⁴
32.	University of Southampton	Highfield, Southampton, UK	Thermal arc beam facility	John Stark

heating the oxygen plasma with argon or helium will increase the kinetic energy of the oxygen atoms.

Another method to produce atomic oxygen is through dissociative ionization of molecular oxygen by electron bombardment using commercially-available ion sources²⁵. The mechanism can be described by:



The ion beams of O^+ and O_2^+ are extracted from the plasma and then accelerated and mass selected by crossed electric and magnetic fields. The selected beam is then decelerated to the appropriate energy and neutralized by one of the following means: electron transfer from flat metal surfaces (grazing incidence neutralization), resonant charge exchange with oxygen atoms by decomposition of heated metal oxides, electron seeding, or resonant charge exchange with gaseous nitrogen or water vapor. Sources using charge exchange methods are good at energies $> 100 \text{ eV}$, however, they suffer from space charge limitations below 10 eV and produce beam intensities orders of magnitude less than other techniques.

Another method for producing fast neutral beams of ground state atomic oxygen is through the production of O^- ions by resonance dissociative attachment in nitrous oxide (N_2O) followed by photodetachment to neutralize the O^- ions.^{17,19} The process of resonance dissociative attachment is described by:



The attractive higher attachment cross section, coupled with the fact that N_2O does not affect indirectly heated cathodes or ion gun filaments as severely as O_2 make N_2O a good gas for O^{-} production. Neutralization of the O^{-} beam can be accomplished by photodetachment within the resonant cavity of continuous wave dye or argon ion lasers, or by a system of mirrors which causes the laser beam to transverse and interact a number of times with the ion beam. Neutral atoms produced this way cannot be focused or calumniated after they exit the neutralizer, and the flux at the target position will depend on the efficiency of the photodetachment process since ions not photodetaching are removed from the neutral beam by a magnetic field and collected by an ion detector.^{11,25}

The plasma techniques discussed above are produced by electric fields having a range of frequencies from constant (dc arcs), < 1 kHz (ac arcs), 20 to 50 MHz (inductive coupling), and 2.5 GHz (microwaves). These sources require some physical device to support the plasma. Direct current arcs require electrodes, rf plasma plasmas require an induction coil, and microwaves require a resonator or waveguide. Because rf and microwave source heating occurs by direct plasma-electric field interactions characterized by large adsorption coefficients with the outer layers of the plasma, these modes of plasma production are characterized by low power densities (< 200 W cm⁻³), modest temperatures (< 8,000 K except for dc arcs—20,000 K). Power

inputs ranging from 15 kW for dc arcs to 100's of watts for rf and microwave sources are required.^{11,25}

Although the fluxes produced by these methods are generally of low intensity, they are well suited for conducting fundamental research on mechanisms leading to surface recession and space glow. Ideally, facilities using these techniques should produce neutral beams of low-to-moderate fluxes which are free of contaminants such as ions, metastable 1S or 1D oxygen atoms, or any other highly reactive species. This objective has not yet been realized, however.^{11,25}

Methods which produce high-intensity beams include laser-induced breakdown of molecular oxygen which is introduced into an evacuated supersonic expansion nozzle through a pulsed molecular beam valve, and laser-driven evaporation of cryogenically-frozen ozone/oxygen films and thin films of indium-tin oxide (ITO) bonded to transparent substrates. The basic concept of laser-induced breakdown is to rapidly introduce a burst of gas into an evacuated nozzle and then focus the output of a pulsed laser to cause a breakdown at the nozzle throat.^{11,25}

A high temperature plasma (15,000 K, depending on the rear gas used) is produced by a laser-initiated detonation wave which then expands through a nozzle specifically designed to allow electron-ion recombination but no atomic recombination. As the high temperature gas expands through the nozzle, its directed velocity increases, and a thermally "cold" high energy beam of oxygen atoms is produced at the nozzle exit. This is schematically shown in figure A-2.^{11,25}

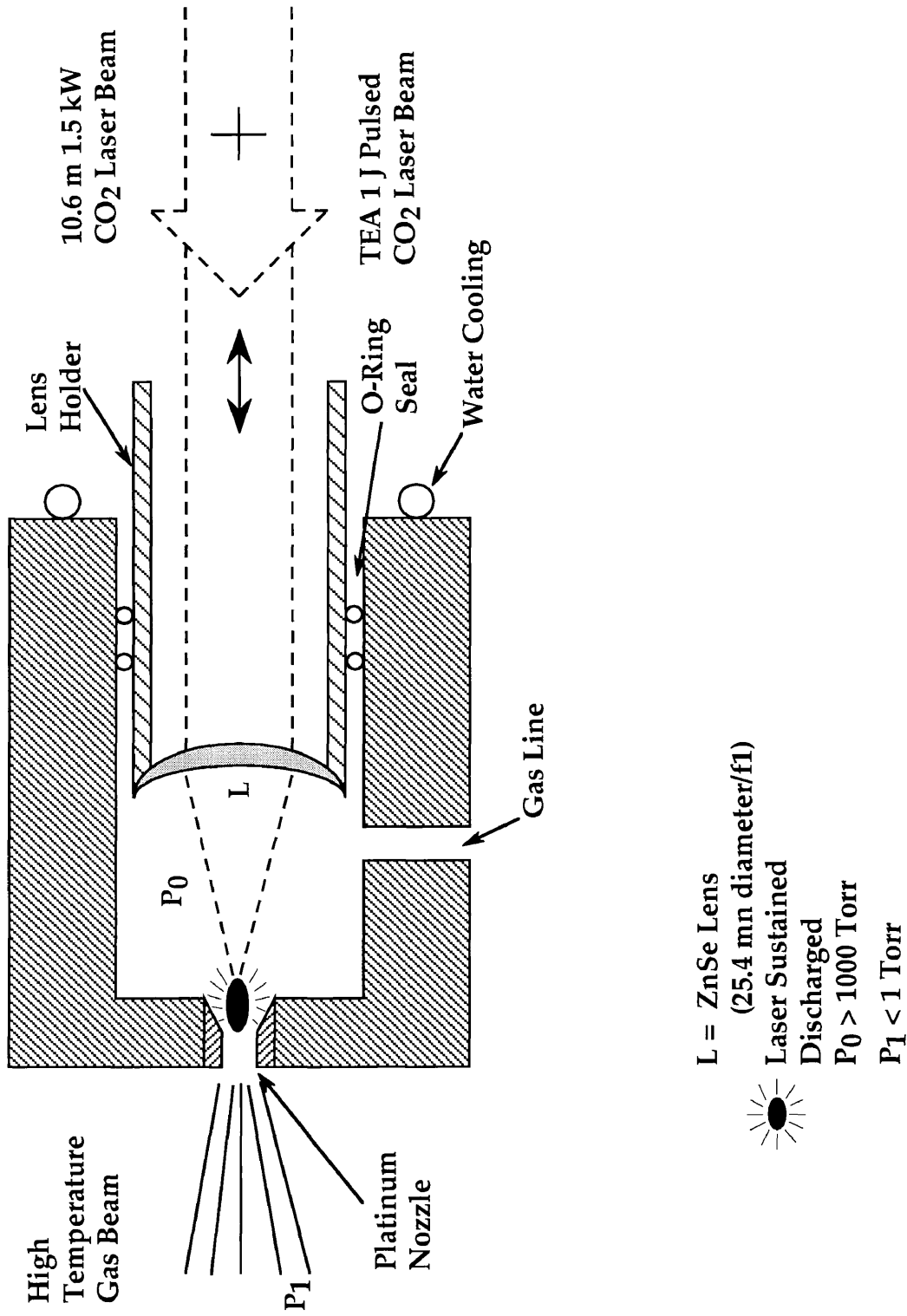


Figure A-2. Diagram of the Atomic Oxygen Beam Generator at Los Alamos National Laboratory

Laser-driven evaporation uses a technique known as laser blow-off to produce pulsed beams of atomic oxygen. A thin coating of cryogenic ozone or ITO is irradiated by a high-energy, pulsed laser directed at the target film from the substrate side. The ITO film or frozen ozone is vaporized in vacuum and an intense pulse of energetic atomic and molecular oxygen (together with metal atoms in the ITO films used) is produced. A chopper is used to separate molecular oxygen and metal atoms from atomic oxygen. Neutral beams made in this way contain very few ions since the ion content of beams produced from rear surface radiated films is greatly reduced compared to beams produced by front surface laser evaporation techniques.^{11,25}

One of the oldest oxygen sources is an RF plasma asher.³⁵ The RF plasma asher can be operated over a fairly wide range of pressures and RF powers producing a wide range of environments. When operating with pure oxygen as the source gas, atomic oxygen yields can vary from 1 to 60 percent, depending on the operating variables. Unless a faraday cage is used to enclose the sample, the sample is exposed directly to the plasma and the RF field. The RF field can be a problem for heat conducting samples or samples containing conducting material because the RF field inductively heats the samples.

An example of a typical RF asher is shown in figure A-3 used by Lerner and Wydeven.¹⁵ The reactor is made of Pyrex glass. An RF generator is placed approximately 15 cm from the molecular oxygen inlet and the net RF power (13.56 MHz) into the reactor typically is maintained at 15W. Oxygen pressures are maintained between 0.05 and 0.55 Torr. The design incorporates a right-angle bend in the pyrex tubing about 40 cm from the oxygen inlet to protect the samples from ultraviolet radiation, ions, and electrons generated

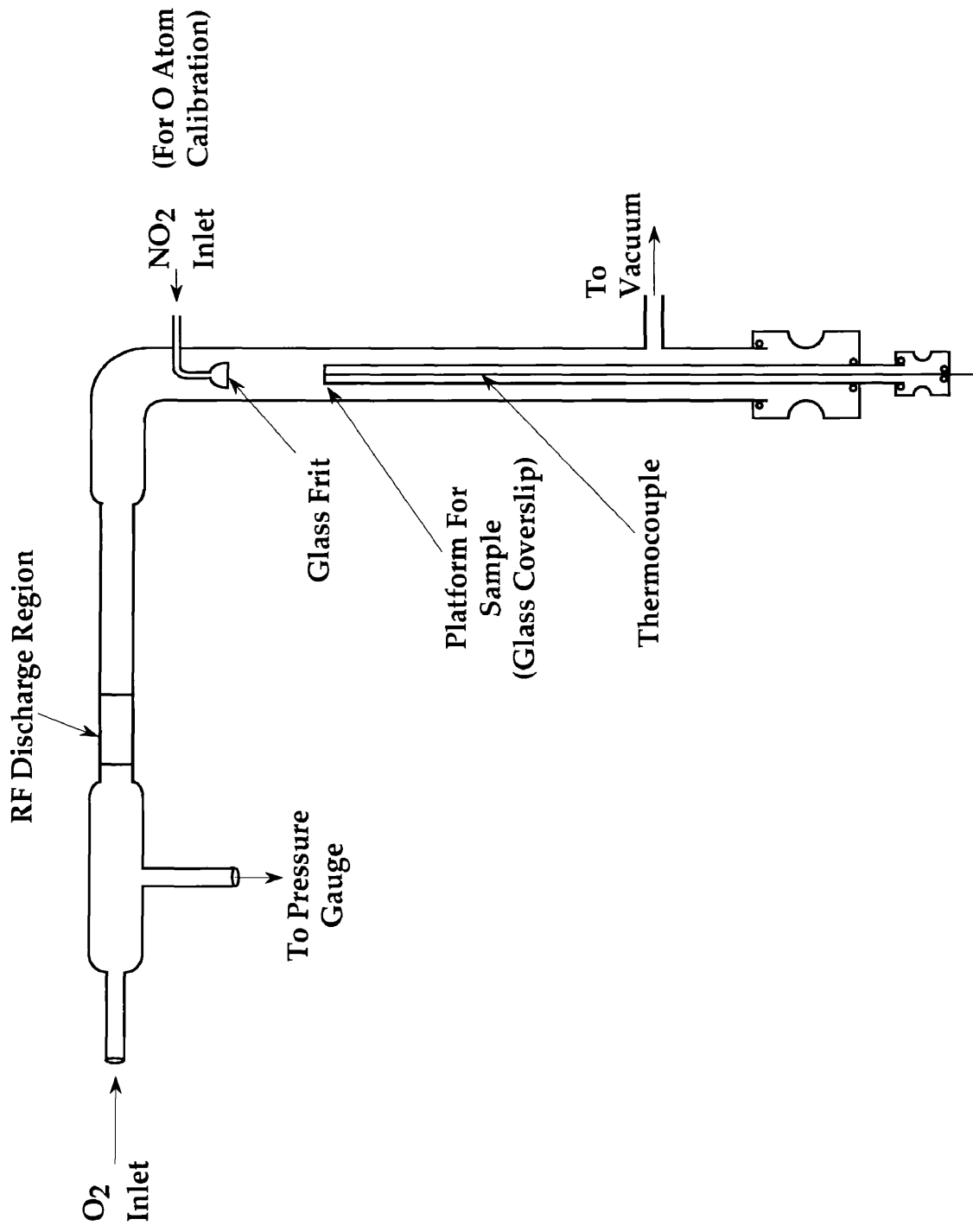


Figure A-3. An RF plasma asher used Lerner and Wydeven at NASA Ames Research Center, Moffett Field, California.

in the plasma. A glass frit placed below the right-angle bend measures the concentration of atomic oxygen by NO_2 titration.

APPENDIX B

DETERMINATION OF THE WORK FUNCTION FOR CIRCULAR THORIA COATED TUNGSTEN AND IRIIDIUM FILAMENTS

1. INTRODUCTION

In order to assure optimum cathode performance, experiments were performed to determine the work function of different cathode materials, specifically, thoria coated tungsten and iridium. It is well known that tungsten is a more stable filament material at low pressures (less than 10^{-6} Torr O₂), but the oxidation rate at higher pressures is quite severe. Iridium was investigated for environments greater than 1×10^{-6} Torr O₂ because it is much less chemically reactive.

The thermal electron emission of a cathode can be describe by the Richardson-Dushman equation:³⁶

$$J_s = A_0 T^2 e^{-\phi / kT} \quad (\text{B-1})$$

where: J_s = saturated thermal emission current density in A cm²
 A_0 = Dushman's constant: theoretical value is 120.4/cm²deg²
 T = temperature in degrees Kelvin
 ϕ = true work function in electron volts (eV)
 k = Boltzmann's constant.

Equation B-1 should be multiplied by the factor $(1 - r)$, where r is the reflection coefficients for electrons with sufficient energy to permit escape from the surface in the absence of an externally applied field. Since the value of r is on

the order of 0.05 for most clean metals, multiplying by the term $(1 - r)$ has little effect on the result.

The value of the work function θ varies linearly with temperature according to:

$$\phi = \phi_0 + \alpha T, \quad (\text{B-2})$$

where ϕ = work function at $T = 0$ K
 α = $d\phi / dT$, the temperature coefficient of the true work function.

The experimental values for α are on the order of 10^{-4} eV/K for most metals. By combining equation (B-1) and (B-2), the following is obtained:

$$J_s = A_0 T^2 e^{-\alpha / k} e^{-\phi_0 / kT}. \quad (\text{B-3})$$

A plot of the experimental values of J_s / T^2 verses $1 / T$ gives a straight line for clean metals and the slope of the line is a measure of ϕ_0 / k and the intercept at $1/T = 0$ gives the value of $A_0 e^{-\alpha/k}$. Table A-1 gives the values for these parameters:

Table 1
Work Function Values for Various Elements³⁶

Element	ϕ_0	$A_0 e^{-\alpha/k}$
Cr	3.0	48
Mo	4.2	55
W	4.5	70
Re	5.1	52
Fe	4.5	26
Ni	4.41	30
Rh	4.80	33

2. FILAMENT CLEANING PROCEDURES

Iridium filaments were cleaned by firing them in air at 1150° C for 15 minutes. The filament turned from a silvery color to a dull grayish color because oxide formation on the filament caused the surface to become rough. The roughened surface area provided a better adhesion of the cataphoretic solution to the filament.

Tungsten filaments were cleaned by boiling the filaments for 5 minutes in a 20% potassium hydroxide solution. The filaments were then rinsed thoroughly in running tap water and then rinsed in three changes of deionized or distilled water at room temperature. The filaments were then dried using a heat gun.

3. COATING PROCEDURES

The cataphoretic solution was purchased from CM Furnaces, Inc. Bloomfield, New Jersey. The solution is composed of 5 g ThO_2 and 0.075 g $\text{Th}(\text{NO}_3)_4$ in 100 ml of 95.7 % ethyl alcohol. The solution was placed in a beaker. A cylindrical molybdenum anode lined the beaker and the filament was the cathode. Direct current voltage of 100 V at a current of 0.5 A was applied for 1 minute. See figure B-1. The coated filaments were air dried.

4. WORK FUNCTION EXPERIMENT

The filament was placed in an unpumped high vacuum chamber, with ultimate pressures in the 10^{-8} (unbaked) and 10^{-9} (baked) Torr range. A diagram of the electrical circuit is shown in figure B-2. The filaments were heated at 1200°C for 15 minutes to remove excess moisture and other contaminants and to activate the ThO_2 coating prior to taking data. The temperature, filament emission current, filament voltage, and filament current were recorded for a constant input voltage. Measurements were taken from high temperatures to low temperature in order to minimize the recontamination of the filament. The temperature and emission current data were used in the Richardson-Dushman equation to determine the work function.

5. RESULTS

Figures B-3 and B-4 are the Richardson plots for the thoria coated tungsten and thoria coated iridium. In both plots there was a break in the straight line at the highest temperatures because of the loss of secondary

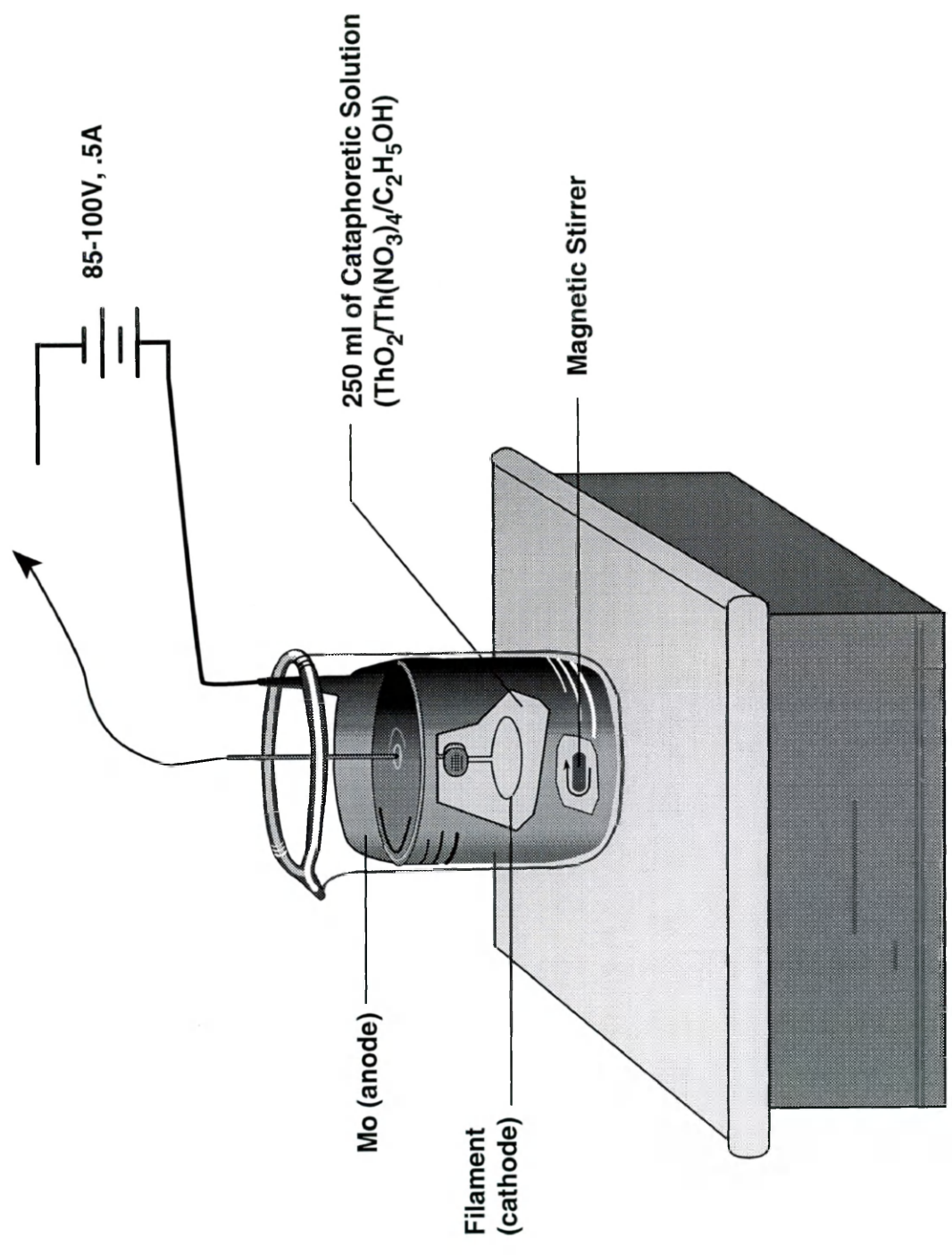


Figure B-1. Diagram of cathaphoretic coating process.

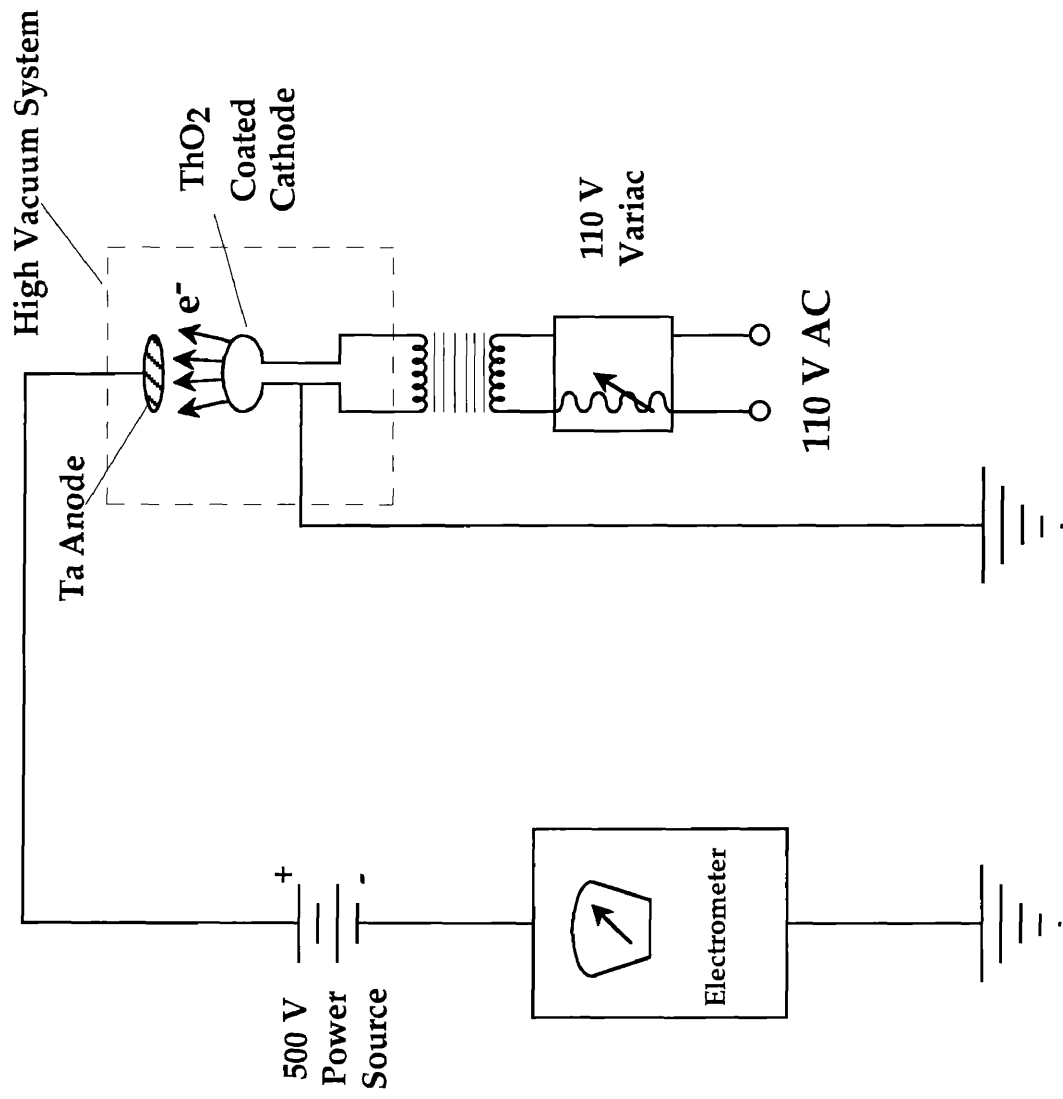


Figure B-2. Electrical diagram of the filament testing apparatus.

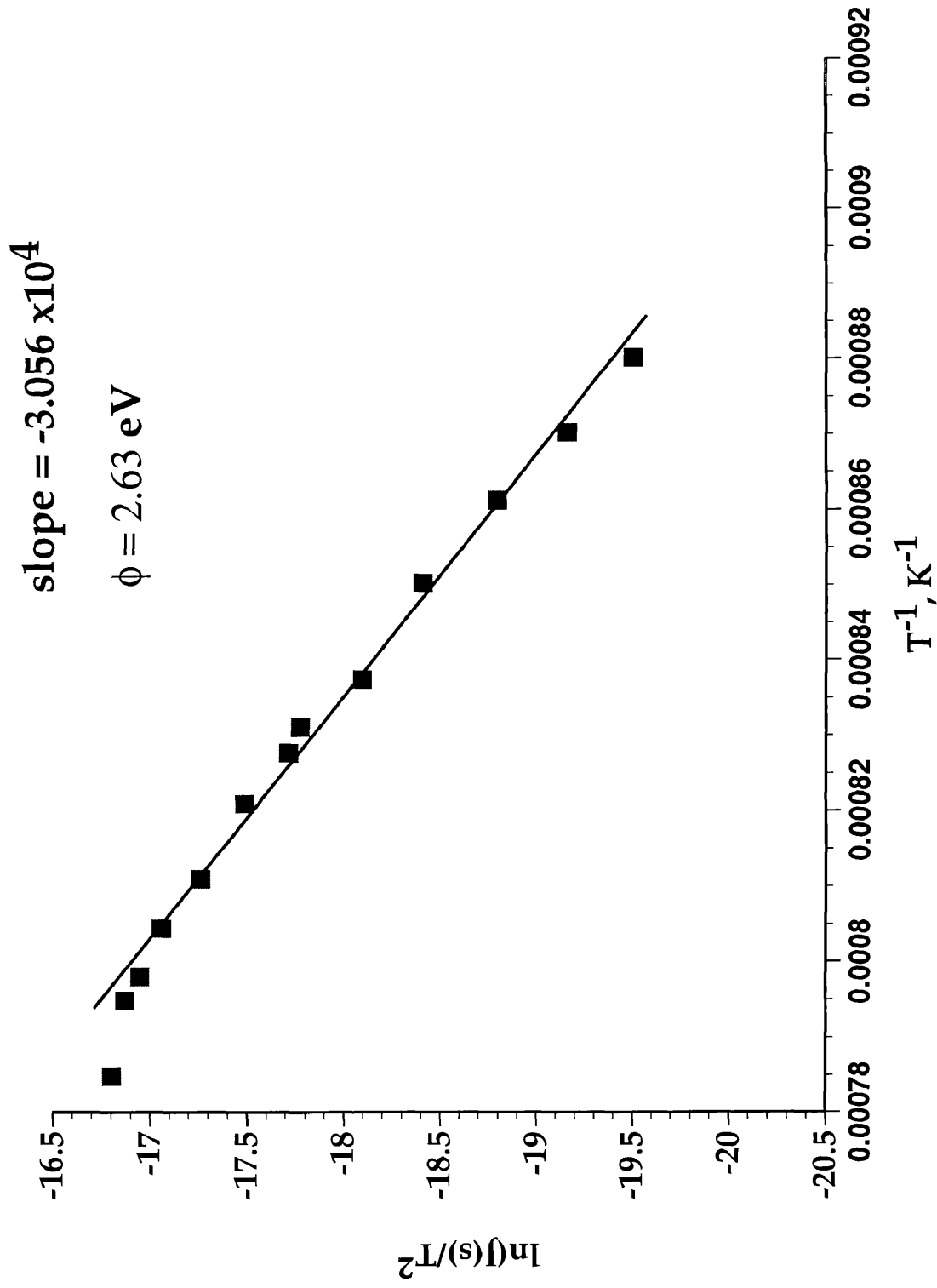


Figure B-3. Work function determination of circular thoria coated tungsten filaments.

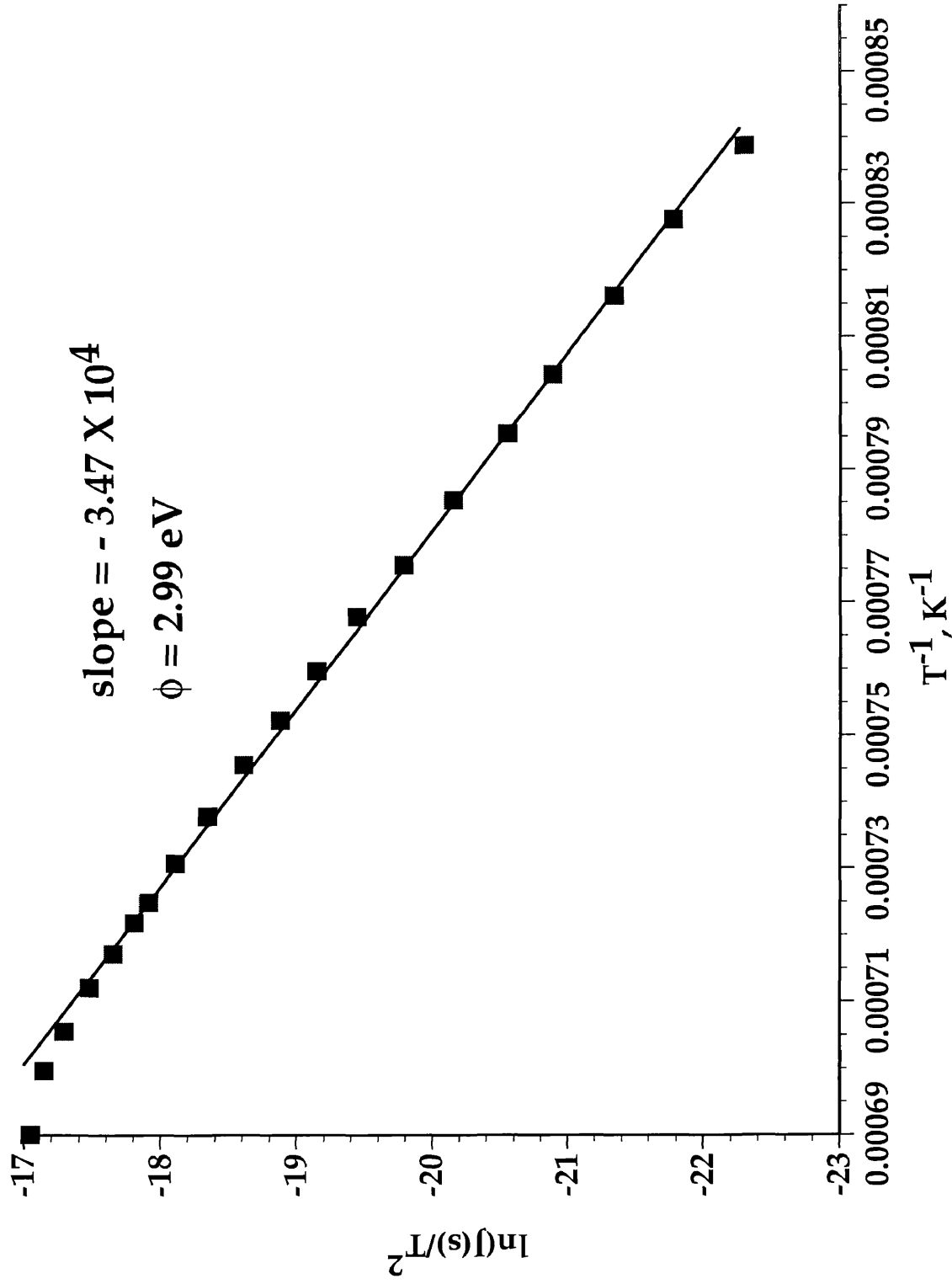


Figure B-4. Work function determination of a circular thoria coated iridium filament.

electrons (no Faraday cup was used) but a sufficient linear region was available to determine a slope. Experiments with uncoated tungsten gave 4.5 eV (which is in good agreement with past research and serves as a calibration of the method). The work function determined for the thoria coated tungsten was 2.6 eV and for the thoria coated iridium was 2.9 eV

Since the work function determined for the thoria coated tungsten was lower than the work function determined for the thoria coated iridium, the former runs at a lower temperature than the latter (for the same emission current). Further, since the former had superior stability, the thoria coated tungsten was chosen as the electron source for the oxygen generator.

In actual operation, it was observed that the oxygen generator with the thoria coated tungsten filament operated at 1300 °C produced the same flux of oxygen atoms as the previous generator did using an uncoated tungsten filament operating at greater than 2000 °C.

APPENDIX C

ION GAUGE AND QUADRUPOLE MASS SPECTROMETER

1. ION GAUGE

An ion gauge was used to measure the total pressure in the characterization system. The gauge is composed of two tungsten filaments, a grid, and an ion collector. The filament generates e^- that are accelerated toward the grid and describe oscillatory paths around the grid until collected. See figure C-1. The rate constant for creating positive ions is greater than the rate constant for negative ions, therefore, more positive ions are generated.³⁷

The pressure P_j is determined by:

$$i^+ = i^- S l_{e^-} P_j \quad (\text{C-1})$$

where i^+ is the number of positive ions produced, i^- is the number of negative ions produced, S is the probability of an ion being formed, and l_{e^-} is the path length of the electron. Since $K = S l_{e^-}$ known as the gauge constant then:

$$P_j = \frac{i^+}{i^- K} \quad (\text{C-2})$$

At the collector, the positive ions bury into the collector lattice. The positive ion is neutralized by the e^- from the Fermi sea of electrons, thus

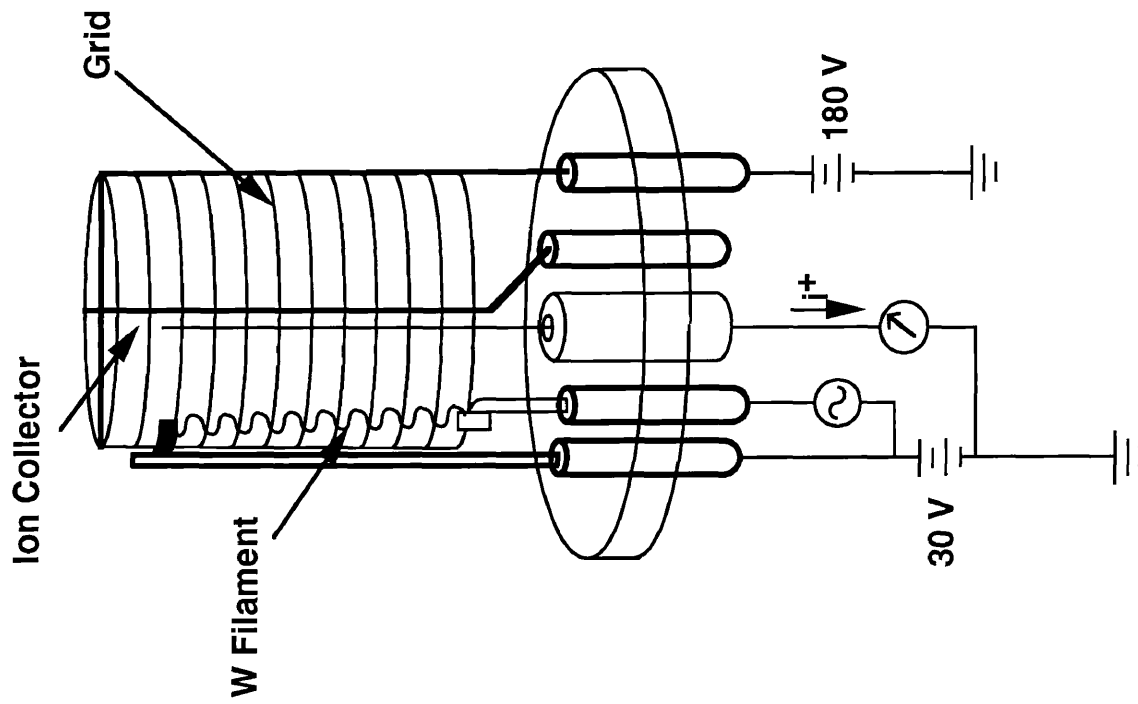


Figure C-1: Schematic of an Ion Gauge

creating an electron current equivalent to the number of ions collected. As indicated in equations (C-1) and (C-2), this current is directly proportional to the pressure.

2. QUADRUPOLE MASS SPECTROMETER

The mass spectrometer used as the detection source in this experiment was a quadrupole mass analyzer manufactured by UTI (Uthe Technology International) model # 100C. The mass analyzer is composed of three parts: the ion source, the mass filter, and the electron multiplier.¹¹ (See figure C-2)

The ion source in the mass spectrometer is very similar to the ion gauge used to measure pressure. It is, also, composed of dual filaments, an open grid, and a reflector; in addition, it has a voltage plate and a focus plate. The purpose of this ion source is to ionize atoms and molecules for analysis in the other sections of the mass spectrometer. The gas molecules within the ionizer are bombarded by electrons from the filaments and become positively charged ions which are then injected into the quadrupole mass filter section. The dual filaments are operated simultaneously with an automatic constant emission control in the event of failure of either filament. Electrons are emitted from the filaments and are accelerated toward the grid. The grid is at a positive potential with reference to the filaments and ground. The electrons which do not strike a grid wire or which do not ionize a substance pass through the grid volume into the region between the grid and the reflector. These electrons are decelerated and reaccelerated back toward the grid due to the electric field produced by the negative reflector voltage and the

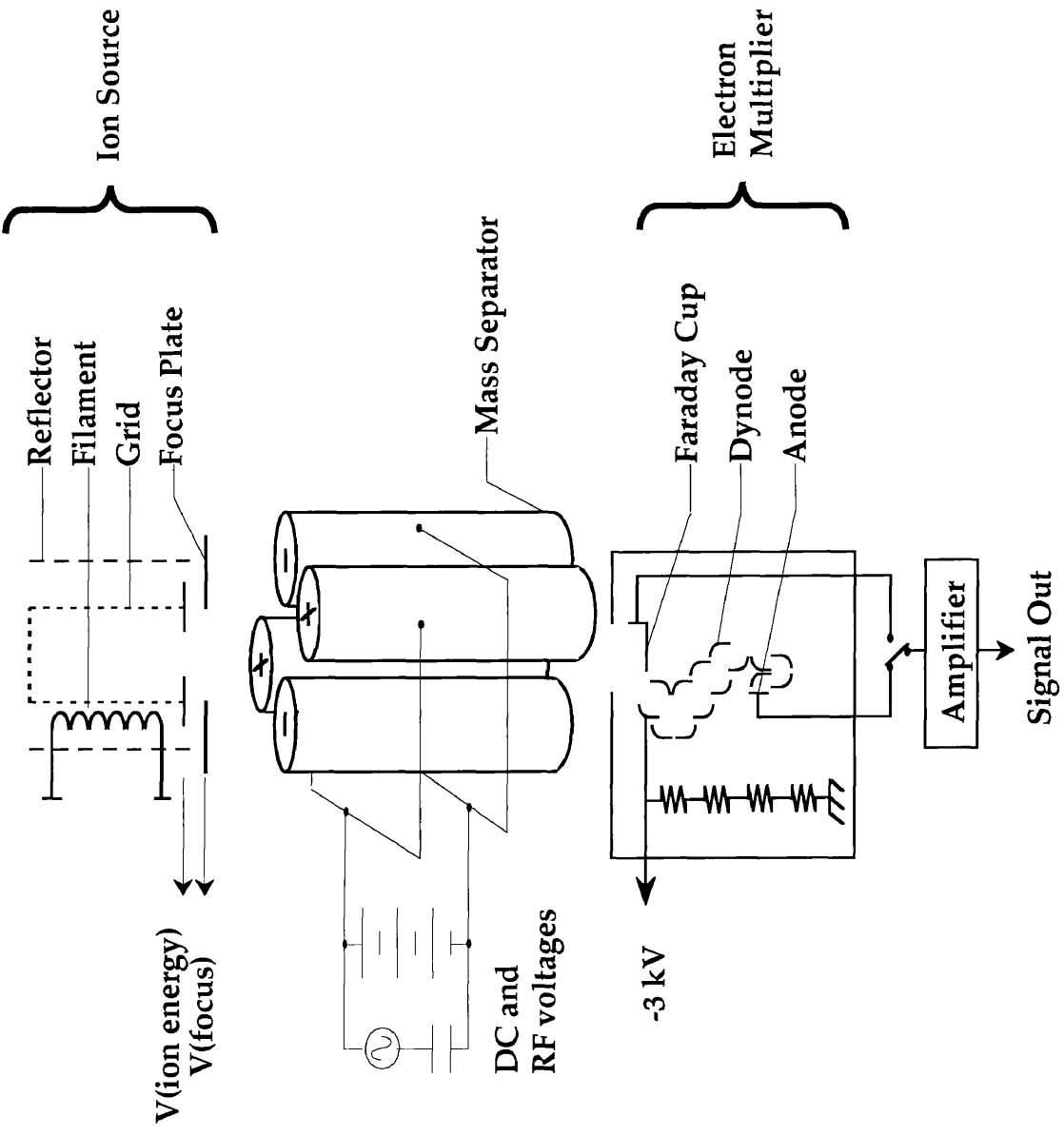


Figure C-2. Schematic of Quadrupole Mass Analyzer

positive grid voltage. Electrons that do not ionize a substance circulate in this field until they are either recaptured or collected by the grid.

A positive ion is formed if sufficient energy is transferred through electron interaction with a neutral atom or molecule. While in the grid volume, the ions are attracted toward the center by the negative potential produced by the increasing electron density toward the center and toward the focus plate. The focus plate is kept at a negative potential (between 0 - 85 V). This provides an initial extraction and some focusing of the ions into the filter section of the mass spectrophotometer.³⁸

The filter section of the mass spectrophotometer is made up of four precisely machined molybdenum rods. The rods are very accurately aligned and attached to alumina insulators which are enclosed in a stainless steel cylinder. Radio frequency (rf) and direct current (dc) voltages are applied to the rods to produce an electrodynamic field to filter the various particle masses. The opposed rods are electrically connected with one pair being attached to the positive side of a variable dc source and the other pair to the negative terminal. The variable radio-frequency ac potential applied to each set of rods is 180° out of phase. Mass scanning is done by varying the potentials of the two sources while keeping their ratio and frequency constant. The potential changes during a typical scan are shown in figure C-3. The two diverging straight lines show the variation of the two dc potentials as a function of time during one scan.³⁸

The combined fields cause the particles to oscillate about their axis of travel. A charged substance with a specific mass-to-charge ratio will have a

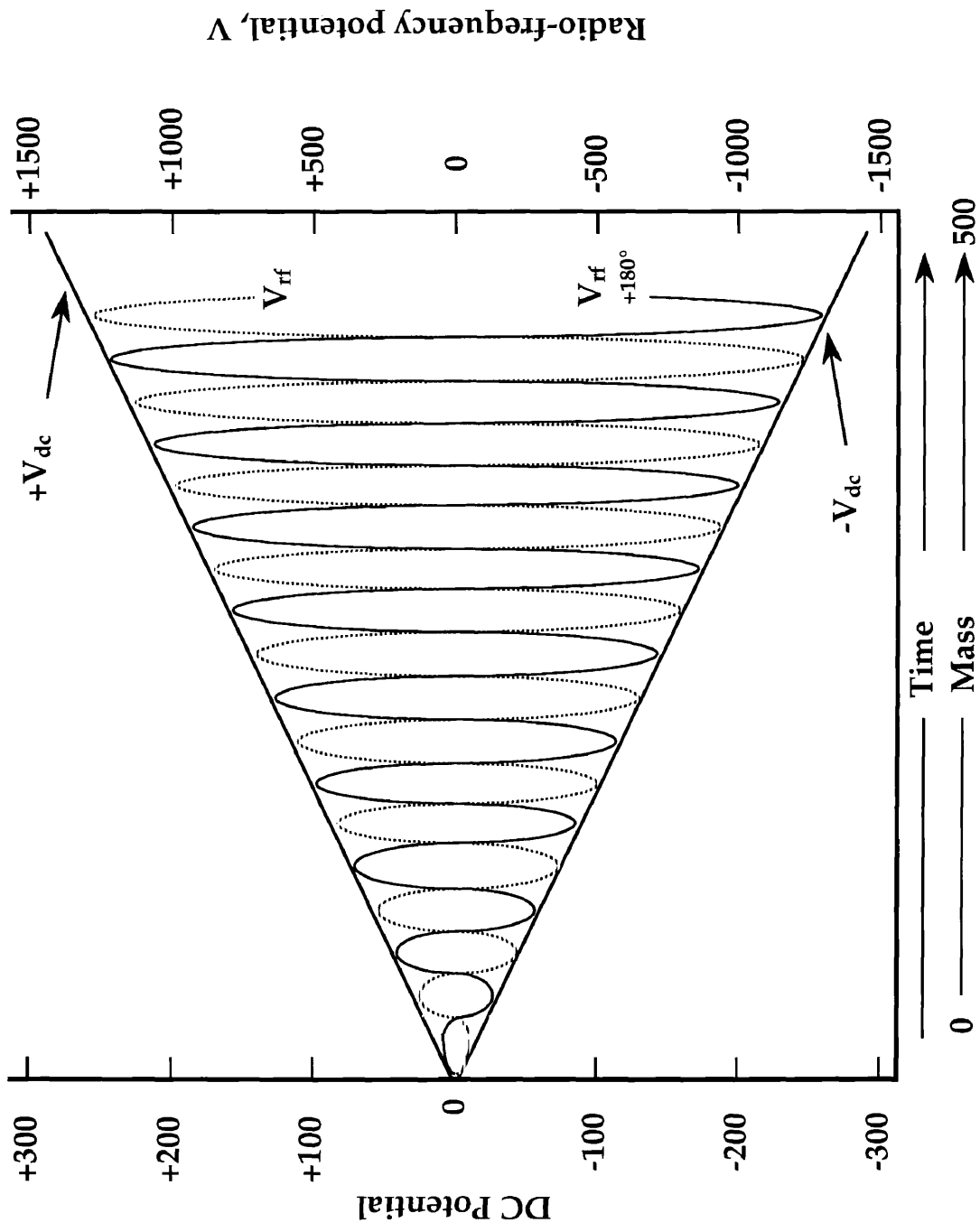


Figure C-3. Voltage relationships of a quadrupole mass analyzer during a scan.

dynamically stable trajectory within the field formed. Particles with different mass-to charge ratios are filtered out by collisions with the rods. By continuously varying the applied voltages, a range of species can be sequentially stabilized and traverse the length of the filter assembly^{11,38}

Once the ions have been filtered through the rods, the ions enter the ion detector and amplifier system. The ion detector is a 16-stage electron multiplier with the first stage being a Faraday cup. The Faraday cup consists of a small electrode surrounded by an open-ended reflecting box that prevents the escape of reflected ions and ejected secondary electrons. The Faraday cup is between -1 and -3 kV.³⁸

Each additional stage is composed of a Cu/Be oxygen activated dynode with a potential difference of about 60 to 200 V between each stage. The ions emerging from the quadrupole filter section are attracted to the first stage by the difference in potential. The impinging ions cause emission of secondary electrons which are then attracted toward the second dynode, and so on down the chain to the anode. Each electron striking a dynode releases between one and two electrons, producing charge multiplications on the order of 10^4 to 10^6 .^{11,37}

VITA

Gilda Ann Newton Miner

Born in San Diego, California, on January 22, 1948. Graduated from Brandon High School in Brandon, Mississippi, May 1966. Received a B.S. in Biology from Christopher Newport College (now Christopher Newport University) in May 1973. Taught 8th grade Physical Science at Huntington Intermediate School in the Newport News City Schools System from January 1973 to June 1980. Began working at NASA Langley Research Center as an apprentice September 1980. Received a B. S. in Chemistry from Christopher Newport College in May 1983. Completed NASA Langley Research Center Apprentice School in October 1983. Began working as a chemist for the Space Technology Branch, Space Systems Division, NASA Langley Research Center March 1984.

FORMAL PUBLICATIONS

1. G. A. Miner, A. K. St. Clair, D. M. Stoakley, M. L. Caplan, C. R. Kalil, C. A. Brown, and E. M. Shipulksi, *Proc. Am. Chem. Soc., Division of Polymeric Materials: Science and Engineering*, **72**, pp 355-6.
2. R. C. Costen, J. H. Heinbockel, Miner, G. A.; W. E. Meador, Jr., B. M. Tabibi, J. H. Lee, and M. W. Williams, *Reduced Dimer Production in Solar-Simulator-Pumped Continuous Wave Iodine Lasers Based on Model Simulations and Scaling and Pumping Studies*. NASA TP-3486, March 1995.

3. W. E. Meador, Jr., G. A. Miner, and J. H. Heinbockel, *Vibrational Relaxation in Hypersonic Flow Fields.*, NASA TP-3367, September 1993.
4. G. A. Miner, and P. D. Babb, *Hazard Calculations of Diffuse Reflected Laser Radiation for the SELENE Program*, NASA TM-4520, October 1993.
5. G. A. Miner, W. E. Meador, Jr., and C. K. Chang, *Initiation Precursors and Initiators in Laser-Induced Copolymerization of Styrene and Maleic Anhydride in Acetone*, NASA TM-4166, March 1990.

REFERENCEABLE ORAL PRESENTATIONS

1. G. A. Miner, and R. A. Outlaw, *Continuous Electron Stimulated Oxygen Atom Emission From Ag Permeation Membranes*. Presented at the American Vacuum Society, Denver, Colorado; October 25, 1994.
2. G. A. Miner, and J. H. Lee, *An Efficient Solar Pumped t-C4F9I Iodine Laser*, Presented at the 8th Interdisciplinary Laser Science Conference, Albuquerque, NM, September 1992.

AWARDS

1. NASA Tech Brief Award for Initiation Precursors and Initiators in Laser-Induced Copolymerization of Styrene and Maleic Anhydride in Acetone. May 1993.
2. NASA Group Achievement Award to Space-Based Beam Power Research Team for outstanding and sustained accomplishments in the development of in-space laser-beamed power technology. March 1992.
3. NASA Special Achievement Award for innovatively and efficiently establishing a polymer chemistry laboratory in the High Energy Science Branch and for performing basic research leading to understanding of key polymerization mechanism. September 1986.
4. Langley Research Center Quality Circle Achievement Award for the establishment of a designated area for ultrasonic contract inspection. November 1984.

5. NASA Special Achievement Award for exceptional dedication and ability in performance of tasks under very difficult and unique work requirements to complete the internal insulation installation in the National Transonic Facility pressure shell. July 1982.